Atmospheric
Chemistry
and Physics

<Open Access>

Hydroxyl airglow observations for investigating atmospheric dynamics: results and challenges

Sabine Wüst[1], **Michael Bittner**[1,2], **Patrick J. Espy**[3], **W. John R. French**[4], **and Frank J. Mulligan**[5]

[1]Erdbeobachtungszentrum, Deutsches Zentrum für Luft- und Raumfahrt Oberpfaffenhofen,
82234 Wessling, Germany
[2]Institut für Physik, Universität Augsburg, 86159 Augsburg, Germany
[3]Department of Physics, Norwegian University of Science and Technology, Trondheim, Norway
[4]Australian Antarctic Division, 203 Channel Hwy, Kingston, 7050 Tasmania, Australia
[5]Department of Experimental Physics, Maynooth University, Maynooth, Co. Kildare, Ireland

Correspondence: Sabine Wüst (sabine.wuest@dlr.de)

Abstract. Measurements of hydroxyl (OH[*]) airglow intensity are a straightforward and cost-efficient method which allows the derivation of information about the climate and dynamics of the upper mesosphere/lower thermosphere (UMLT) on different spatiotemporal scales during darkness.

Today, instrument components can be bought "off-the-shelf" and developments in detector technology allows operation without cooling, or at least without liquid nitrogen cooling, which is difficult to automate. This makes instruments compact and suitable for automated operation.

Here, we briefly summarize why an OH[*] airglow layer exists, how atmospheric dynamics influence it and how temperature can be derived from OH[*] airglow measurements.

Then, we provide an overview of the scientific results regarding atmospheric dynamics (mainly gravity waves (GWs) but also planetary waves (PWs) and infrasound) achieved with OH[*] airglow measurements. We focus on long-term ground-based OH[*] airglow measurements or airglow measurements using a network of ground-based instruments. The paper includes further results from global or near-global satellite-based OH[*] airglow measurements, which are of special importance for characterizing the OH[*] airglow layer. Additionally, the results from the very few available airborne case studies using OH[*] airglow instruments are summarized.

Scientific and technical challenges for the next few years are described.

1 Introduction

At present, nocturnal hydroxyl (OH[*]) airglow measurements have been performed from ground, aircraft, balloon, ship, rocket, and space. Ground-based OH[*] airglow observations are far more cost-effective than measurements from aircraft and satellite. They have been made since the 1950s and are well suited to long-term studies if calibrations are well maintained, and changes or replacements in the measurement equipment over the years are handled with care and are well documented. More recently, satellite-based and airborne measurements have been carried out. The former measurements are never affected by clouds while the latter ones are not severely affected. Satellites provide global or near-global data; aircraft provide the greatest spatial flexibility. Balloon-borne measurements, as presented recently by Wang et al. (2021), are also not affected by clouds, but the position of the instrument's field of view (FoV) at the OH[*] airglow layer height strongly depends on the wind at the balloon height.

The natural phenomenon of the OH[*] airglow is due to different rotational–vibrational transitions of the excited hydroxyl molecule, which emits radiation between ca. 0.6 and 4.5 µm. Table 1.1 of Khomich et

al. (2008) provides an overview of the principal airglow emissions, including OH*. Additionally, the Skycalc model described in Noll et al. (2014) and available at https://www.eso.org/observing/etc/bin/gen/form?INS.MODE=swspectr+INS.NAME=SKYCALC (last access: 12 December 2022) can be used to show the airglow spectrum in an individual spectral range.[1] The brightest OH* airglow transitions appear in the near infrared around 1500 nm (Rousselot et al., 2000). Populations of some low rotational levels are approximately in local thermodynamic equilibrium. From those, kinetic temperature can be estimated. Even if kinetic temperature cannot be derived, the OH* airglow can be used as dynamical tracer.

The OH* airglow forms a layer in the upper mesosphere/lower thermosphere (UMLT). Often, height and full width at half maximum (FWHM) are given as 87 and 8 km, respectively, referring to Baker and Stair (1988). Those authors summed up results from 34 rocket flights at mid- and high latitudes, which were conducted by different experimenters. They derived 86.8 ± 2.6 km for the altitude of the peak and 8.6 ± 3.1 km for the thickness of the OH* airglow layer. Both parameters can vary (in the case of the centroid height by some kilometres) over several days or even during a single night due to strong dynamics (e.g. changes in the residual circulation during a stratospheric warming or strong tidal motions). These variations also depend on latitude and season amongst others (Grygalashvyly et al., 2014). Peak and centroid height differ slightly since the OH* airglow profile is not completely symmetric: the layer fraction above the peak height is larger than that below (Moreels et al., 1977) and the emission rate profile can be modelled by an asymmetric Gaussian distribution with a wider top part and a narrower bottom part (Khomich et al., 2008). However, this asymmetry is not significant for most applications, and if derived from satellite limb measurements, in most cases smeared out at least in part due to the size of the instrument's FoV. Long-term satellite-based investigation of a larger geographical region (52° N–52° S; Wüst et al., 2020 and references therein) confirm the mean height values of Baker and Stair (1988), although there is some geographical variation.

Amongst others, the height of the emission peak depends on the exact vibrational level: adjacent vibrational levels are separated by some 100 m up to 1 km (Baker and Stair, 1988; Adler-Golden, 1997; von Savigny et al., 2012; Grygalashvyly et al., 2014). If one refers to different vibrational transitions, one therefore obtains information weighted toward different heights. In contrast, a zenith-viewing instrument which spectrally integrates over different vibrational transitions, receives its signal from a greater height range than one which observes an individual vibrational transition.

The OH* airglow measurements are often referred to as mesopause measurements. This is strictly speaking only valid during summer since the mesopause changes in height by ca. 14 km during the year: it reaches ca. 86 ± 3 km in summer (approximately May–August in the Northern Hemisphere according to She et al., 2000) and ca. 100 ± 3 km in winter (rest of the year). Based on lidar measurements for different latitudes (Lübken and Von Zahn, 1991; She et al., 1993; Von Zahn et al., 1996) and models (Berger and Von Zahn, 1999), this mesopause height variation is a worldwide phenomenon. However, the OH* centroid height varies by only a few kilometres, so OH* airglow measurements sample the UMLT in different seasons. This means that the OH* airglow layer lies in a height region with a small vertical temperature gradient during summer and a negative vertical temperature gradient during winter. This has direct consequences, e.g. for the estimation of the mesopause temperature trend or the Brunt–Väisälä frequency based on OH* airglow temperature measurements.

Ground-based and airborne measurements integrate over the OH* airglow layer profile. Thus, vertically resolved information is not available or only to a very limited extent (as already mentioned above using different vibrational levels). Satellite-based limb-scanning instruments can provide vertically resolved profiles of the OH* volume emission rate (VER). There is a large number of different ground-based instruments used for OH* airglow observations all over the world. Several stations are loosely working collaboratively in the coordinated Network for the Detection of Mesospheric Change (NDMC, https://ndmc.dlr.de, last access: 12 December 2022). The largest subgroup of technical identical OH* spectrometers in the NDMC are of the GRIPS (Ground-based Infrared P-branch Spectrometer) type. These instruments were developed at the University of Wuppertal in the late 1970s. In the 2000s, the instruments were redesigned by the German Aerospace Centre (DLR) and the University of Augsburg (UNA) to take advantage of the technical developments in semi-conductor technology. This has allowed operation without liquid nitrogen cooling and an order of magnitude improvement in temporal resolution. As for most instruments in the present era, the retrieval algorithm was designed and standardized to facilitate automated operation. This has enabled the simultaneous operation of several instruments as a group to view a contiguous atmospheric region, such as the Alpine region where seven GRIPS instruments are currently deployed and contribute to the Virtual Alpine Observatory (VAO, https://www.vao.bayern.de, last access: 12 December 2022). The Spectral Airglow Temperature Imager (SATI) is another type of OH* instrument, in this case imagers, which is deployed at several sites (Sargoytchev et al., 2004). It is

---

[1] This model was developed for astronomers. In order to use it for the derivation of OH* airglow information, remove the tick at "Optional parameter initialization using Almanac Service" and select "Emission lines of the upper atmosphere" as well as "Airglow/residual continuum". The model includes the van-Rhijn effect (through "Altitude of target above horizon" or "Airmass") and some variations with month and night. Additionally, you can include the influence of the sun and of precipitable water vapour on the airglow lines (which is especially important at ca. 1.4 and 1.9 µm, see also Smette et al., 2015).

a complete redesign of an older instrument called MORTI (Mesopause Oxygen Rotational Temperature Imager), which was not sensitive to OH* (Wiens et al., 1997). Beside adding the OH* channel, the cryogenic cooling was replaced by a thermoelectric one, temperature and emission rate are read out in real time, and it can be operated remotely. SATI is a Fabry–Perot interferometer.

As for the satellite-based limb-scanning instruments, there are a few of them currently in orbit and providing measurements for many years: SABER (Sounding of the Atmosphere using Broadband Emission Radiometry, Russell III et al., 1999) on TIMED (Thermosphere Ionosphere Mesosphere Energetics Dynamics); OSIRIS (Optical Spectrograph and InfraRed Imager System, Llewellyn et al., 2004) on Odin; and MLS (Microwave Limb Sounder, Waters et al., 2006) on EOS (Earth Observing System) Aura (which is somehow extraordinary since it measures the lowest possible rotational transition of OH*, OH* is not vibrationally excited), for example.

This report provides an overview of results focussing on dynamics derived from long-term OH* airglow measurements, but also includes measurements from a larger spatial domain, i.e. using multiple instruments, in Sect. 4. This overview and today's technical and computational development is the basis for identifying possible questions of future research outlined in Sect. 5. Before doing that, the main processes leading to the formation of the OH* airglow layer and the response of the OH* airglow layer to dynamical disturbances are summarized in Sect. 2. The principle of the temperature derivation is outlined in Sect. 3.

2 The OH* layer

2.1 An overview of OH* production and loss mechanisms in the UMLT

Excited OH molecules are produced by different reactions in the UMLT. A comprehensive overview is given by Khomich et al. (2008) in their Chapter 2.2.
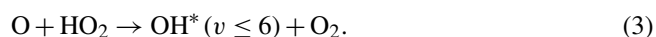
The first two reactions were proposed in the early 1950s – the ozone–hydrogen reaction (Bates and Nicolet, 1950; Herzberg, 1951; Heaps and Herzberg, 1952),

$$O_3 + H \rightarrow OH^* (v \leq 9) + O_2 + 3.34 \text{ eV}, \tag{1}$$
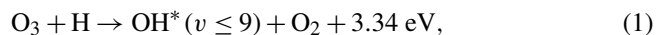
and the oxygen–hydrogen reaction (Krassovsky, 1951),

$$O_2^* + H \rightarrow OH^* + O, \tag{2}$$

were followed by the perhydroxyl–oxygen reaction in the 1960s (Krassovsky, 1963; Nicovich and Wine, 1987; Nicolet, 1989):

$$O + HO_2 \rightarrow OH^* (v \leq 6) + O_2. \tag{3}$$

Today, at least Eq. (1) is considered. Additionally, some authors also take or took Eq. (3) into account (e.g. see Snively

et al., 2010 and Grygalashvyly et al., 2014). Its necessity but also the vibrational levels which can be populated by this reaction are the subject of some discussions as outlined, for example, by Xu et al. (2012) in their introduction.

Vibrationally excited OH molecules (vibrational level $v \leq 9$) emit radiation in the spectral range of ca. 0.6–4.5 µm. In general, vibrational transitions are accompanied by rotational transitions (e.g. Andrews, 2000), which are less energetic. The rotational transitions split into the P, Q, and R branches, depending on the change of the quantum number of the total angular momentum J. The P branch is the branch with lowest energy and the R branch is the one with the highest; the Q branch is in between. Hence, for emission, as it is the case for the topic of this work, ΔJ increases through the rotational transition by 1 for the P branch, decreases by 1 for the R branch, and stays constant for the Q branch. In the following paragraph, the focus is on the vibrational transitions; rotational transitions will be addressed again in Sect. 3, in the context of rotational temperature derivation.

In general, the ozone–hydrogen reaction is regarded as the most important one for the generation of OH* (Brasseur and Solomon, 1986; Grygalashvyly, 2015 and citations therein), reaching vibrational levels of up to 9. Lower levels are populated by spontaneous emission through the following:

$$OH^* (v') \rightarrow OH^* (v'') + h\nu, \tag{4}$$
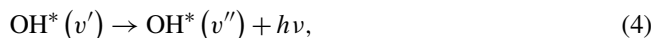
where $v' > v''$, or by collisional relaxation as addressed later by Eq. (6).

Since only the ozone–hydrogen reaction is able to populate the higher vibrational states (e.g. $v' > 6$), modelling OH* intensity can be simplified by focusing, for example, on the OH(8-3) band, leaving out the perhydroxyl–oxygen reaction, rather than on the OH(4-2) or OH(3-1) bands, which are frequently measured.

From the ozone–hydrogen reaction, it becomes clear that the OH* concentration strongly depends on the availability of O_3 and H.

Ozone (O_3) is produced by a three-body-collision reaction of O and O_2 as well as a collision partner which facilitates the reaction but remains unchanged afterwards. Due to the composition of the Earth's atmosphere, the collision partner is N_2 in most cases. The number density of N_2 and O_2 decreases exponentially with height in the homosphere, however, atomic oxygen shows a different behaviour (see Fig. 1a and b, left panel, for the distinction between day and night and a greater height range). It is generated by the dissociation of O_2 and follows a Chapman layer very well above 80 km in height (e.g. Swenson and Gardner, 1998; for a consideration of the altitude range of up to 220 km, see Rodrigo et al., 1991). A Chapman layer is driven by the availability of radiation, which is high above the peak of the Chapman layer and decreases with decreasing height due to absorption. This radiation interacts with an absorber, in this case O_2, whose density is high below the peak and decreases with greater heights (e.g. see Andrews, 2000 for the explanation

of a Chapman layer). The peak of this atomic oxygen layer is above 90 km in height and shows a strong gradient below (Smith et al., 2010). The availability of the different reaction partners leads to the formation of an O_3 layer in the UMLT.

The number density of H reaches its maximum between 80 and 100 km (Fig. 1a and b, left panel). Below a height of ca. 90–95 km, the number densities of H and O_3 fluctuate around each other. The relative variation of O_3 and H shown in Fig. 1a and b (left panel) illustrates why OH* forms a layer in the UMLT. This layer is approximately Gaussian (see e.g. Fig. 1 in Swenson and Gardner, 1998).

The produced OH* has a very short lifetime,[2] it takes less than 1 s before it relaxes through collision (so in this case, the excess energy is transferred to heat, for orientation: the collisional frequency near the mesopause is in the order of $1 \times 10^4 \, s^{-1}$, e.g. Sheese et al., 2011) or through spontaneous emission of infrared radiation via Eq. (4) (Swenson and Gardner, 1998). Additionally, it can be deactivated by chemical reaction with atomic oxygen:

$$OH^* + O \rightarrow O_2 + H. \tag{5}$$

This process mainly occurs on the top side of the layer, where the availability of atomic oxygen is higher than on the bottom side.

Due to increasing air density with decreasing height, collisional quenching with molecules of the surrounding atmosphere becomes more probable on the bottom side and dominates the loss term there (in the following equation, the surrounding atmosphere is denoted by M which typically is molecular nitrogen, or molecular or atomic oxygen):

$$OH^* \left(v'\right) + M \rightarrow OH^* \left(v < v'\right) + M. \tag{6}$$
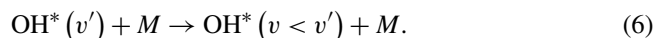
Quenching by atomic oxygen (Grygalashvyly, 2015; von Savigny and Lednyts'kyy, 2013) may be supplemented by multi-quantum collisional deactivation with molecular oxygen (von Savigny et al., 2012 and references therein) and is the reason why emission peak altitudes of OH* emissions from adjacent vibrational levels differ on average by ca. 400–700 m (Baker and Stair, 1988; Adler-Golden, 1997; von Savigny et al., 2012; Noll et al., 2016).

This was a qualitative explanation for the existence of the OH* layer in the UMLT. Grygalashvyly (2015), for example, introduces several analytical approaches to OH* layer parameters.

Until this point, neither dynamical processes which transport species needed for the OH chemistry nor possible variations in the availability of the different constituents due to solar radiation are considered (e.g. during 1 d, see Lowe et

---

[2]The Einstein coefficient for the transition from the 9th to the 7th or the 8th to the 6th vibrational levels, for example, are larger than $10^2 \, s^{-1}$ (Marsh et al., 2006), so the lifetime of the corresponding state is smaller than 10^{-2} s. A summary of the majority of published Einstein coefficients for the different OH* vibrational transitions is available in Table 2.3–2.13 in Khomich et al. (2008).
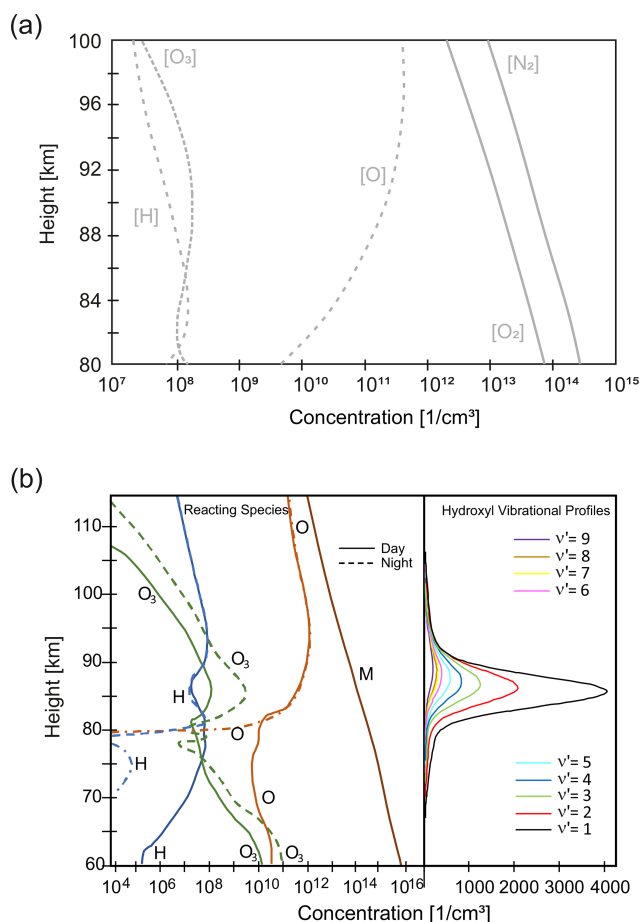

Figure 1. **(a)** Number density of the two major (O_2 and N_2, solid lines) and the three minor (O_3, O, and H, dashed lines) species involved in the production of OH* between 80 and 100 km height following Swenson and Gardner (1998) according to MSIS-90. Relatively large uncertainties exist for the number density of atomic oxygen (Richter et al., 2021), which also shows seasonal variations (e.g. see Fig. 2.15 in Khomich et al., 2008). **(b)** Left panel: vertical profiles of the major-reacting species in the OH photochemical scheme for daytime (solid) and nighttime (dashed) conditions between 60 and 115 km height, M denotes a collisional partner (reproduced from Battaner and Lopez-Moreno, 1979). Right panel: modelled OH* profiles for $v' = 1$–9 (adapted from Xu et al., 2012).

al., 1996 for the behaviour of the OH* layer post sunset). Since the focus of this paper is on dynamical processes, only the first aspect is addressed in the following section.

A good overview of models of wave interactions with OH chemistry is given by Snively et al. (2010) in their Sect. 1.3.

2.2 Influence of atmospheric dynamics on the OH* airglow layer characteristics

The UMLT is dynamically driven over the year by the residual circulation, which is due to an interaction between gravity waves (GWs) and the mean flow, and on temporal scales

of weeks to minutes by different atmospheric waves (planetary waves (PWs), tides, gravity waves, and acoustic waves). All these processes influence advection, modifying the density of the respective species, as well as the temperature that changes the chemical reaction rates. Each of the dynamical processes does this on different temporal scales.

The reacting species for the ozone–hydrogen reaction, O_3 and H, but also OH* itself have relatively short lifetimes in the UMLT, but they still differ by an order of magnitude (ca. 4–6 min for O_3 and H, and less than 1 s for OH*, e.g. Snively et al., 2010 and Swenson and Gardner, 1998). This means that OH* decays before it can be transported substantially. Regarding O_3 and H, transport depends on the period of the disturbance: if it is in the range of the lifetime of O_3 and H (such as gravity waves with frequencies in the vicinity of the Brunt–Väisälä frequency or acoustic waves), advection needs to be taken into account (e.g. see Inchin et al., 2020, who also use the chemical model of Snively et al., 2010 for acoustic waves).

Ozone arises from O and O_2. Both of their lifetimes are considerably different from those of H and O_3: for O, the lifetime exceeds 1 d at the UMLT (Brasseur and Solomon, 1986). Since there is less O than O_2 available between 80 and 100 km (Fig. 1a) and O has a steeper vertical gradient than O_2, O controls the formation of O_3. In their Fig. 7a, Swenson and Gardner (1998) show the individual contributions of O, O_2, and the temperature to the vertically resolved volume emission rate (VER) of OH(8-3). So, dynamical processes leading to vertical transport within 1 d or less can change the O concentration with height and influence the formation of O_3, and in turn, the generation of OH*. The downward transport of O leads to a lower centroid height and a brighter and thicker OH* airglow layer (e.g. Liu and Shepherd, 2006).

Concerning the vertical transport in the UMLT, the residual circulation plays a prominent role. Accordingly, analyses of the OH* airglow layer height reveal an annual cycle. It is more pronounced at higher latitudes than at lower ones (Wüst et al., 2020). A semi-annual cycle is also often found. It is either attributed to physical mechanisms, especially at low latitudes (von Savigny and Lednyts'kyy, 2013), or treated as an analysis artefact, which is necessary to compensate for the fact that the annual cycle does not correspond exactly to a sine wave. Grygalashvyly (2015) provided a good overview about the different characteristics together with explanation of their origins in his Sect. 3. Becker et al. (2020) estimated the effect of gravity waves with a horizontal wavelength of up to 1000 km in height and number density of the OH* airglow layer using model studies.

Due to the strong vertical gradient of O, the maximum perturbation of the OH(8-3) VER is ca. 2–4 km below the peak of the OH* layer (measured, for example, by Lowe et al., 1996 and calculated, for example, by Swenson and Gardner, 1998). The height of the maximum rotational temperature perturbation, however, can be found relatively close to the peak height of the OH* layer. This means that if the OH*

intensity is measured and rotational temperature is derived from these measurements, both signals originate from different altitudes. This leads to a phase shift for dynamical features derived from temperature and intensity time series.

Rotational temperature and intensity derived from a ground-based instrument looking into the sky are always integrated and therefore averaged over the OH* layer profile. Swenson and Gardner (1998) showed that perturbations of this rotational temperature and of the measured relative intensity differ only by a factor, which they called g_T in the description of the rotational temperature perturbation and g_{OH} in the case of relative intensity. The first factor (g_T) depends on the temperature profile (which varies during the year) amongst others, while this is not the case for g_{OH} which is determined by parameters of the OH* layer only. These factors can be interpreted as height-dependent weights, which significantly influence the averaging of the respective signal over the OH* layer. Their different variation with height (see Fig. 2) is the reason that the observed relative amplitude of a disturbance depends on whether one investigates rotational temperature or intensity. For gravity waves with long vertical wavelengths (> ca. 20 km, or high horizontal phase speed > ca. 65 m s^{-1}), the relative intensity perturbation is larger while the relative temperature perturbation is smaller than the true atmospheric density perturbation. Furthermore, time series of intensity measurements are more suitable than time series of rotational temperatures for the study of shorter vertical wavelengths (or slower gravity waves).

3 Measurement techniques for OH* intensity and derivation of temperature

The first measurements of the OH* airglow were performed in the visible range by ground-based instruments as early as the 1920/30s by Babcock, Slipher, and Sommer, as mentioned by Meinel (1950b). However, an identification of the peaks was not possible during that time due to the poor spectral resolution of the spectrogram measurement. In the following years, the observation techniques improved and the existence of OH molecules in the atmosphere was discussed (for an overview see Chapter 2.2.1 of Khomich et al., 2008). During 1949–1950, Meinel operated a spectrograph based on photo plates at Yerkes Observatory (42°34′13″ N, 88°33′23″ W) which he exposed to the night sky for 4 h. He experimentally confirmed that the spectral lines were rotational–vibrational transitions of the OH* molecule (Meinel, 1950b) and calculated a temperature from them (Meinel, 1950a).

In the vast majority of cases, ground-based instruments deliver vertically integrated values of the OH* airglow VER. If the instruments have the required spectral resolution and local thermodynamic equilibrium (LTE) conditions in the emitting region are fulfilled, information about the kinetic temperature, which is naturally weighted by the OH* VER,
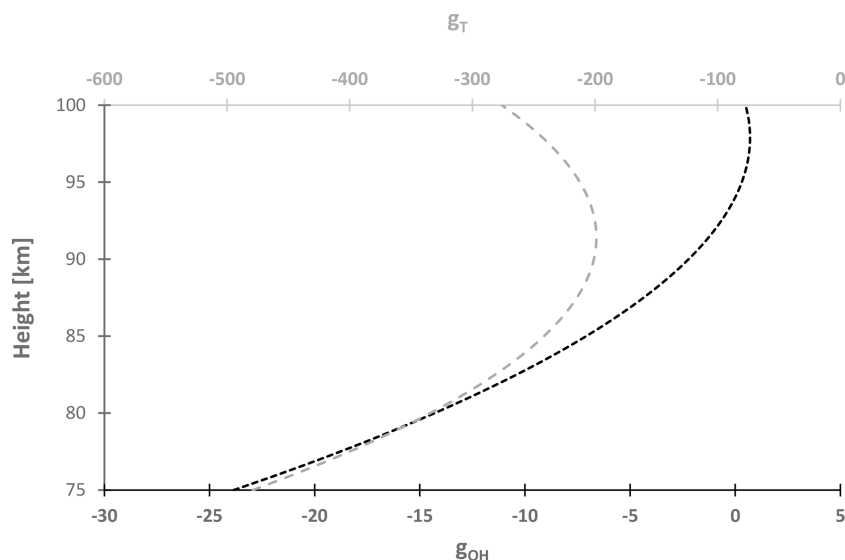
Figure 2. Height-dependent development of g_T (grey) and g_{OH} (black) according to the formulas (42) and (29) of Swenson and Gardner (1998) calculated for January: while g_{OH} decays nearly linearly to zero, this is not the case for g_T. Among other arithmetic operations, these factors are multiplied by the relative density perturbation and the undisturbed VER in order to derive the rotational temperature and the relative intensity perturbation. So, it becomes clear that relative intensity perturbations suffer less from averaging effects than the rotational temperature perturbation.

can be derived. The first criterion is a technical requirement, whereas the second criterion depends on the individual OH* rotational–vibrational transition.

Generally speaking, the assumption of LTE is valid for vibrational and rotational modes below a height of ca. 60 km (Andrews, 2000). Above this height, the relation of the times needed for spontaneous relaxation of a transition and relaxation due to collision needs to be investigated in more detail: for LTE, the mean time between two collisions has to be much shorter than the lifetime for radiative decay. In general, the lowest rotational populations of the lower OH* vibrational transitions are sufficiently close to LTE for a reliable estimate of the kinetic temperature (e.g. see Sivjee, 1992, Pendleton Jr et al., 1993, and references therein, or Noll et al., 2020, who in their Fig. 13 provide an estimate of non-LTE contributions to some rotational temperatures based on their own work and the work of Oliva et al., 2015).

The temperature T_{rot} can be calculated from two different lines (Meinel, 1950a; Baker, 1978; Baker et al., 1985). The basis of this calculation is the following relation for the volume emission rate I (in photons s^{-1} cm^{-3}) for spontaneous emission:

$$I_{(v',J' \to v'',J'')} = N_{v',J'} A_{(v',J' \to v'',J'')}, \quad (7)$$

where v and J are the vibrational and rotational levels, respectively, primed values denote the initial (so-called upper) state, double primed values denote the final (so-called lower) state. The number density of molecules (in cm^{-3}) in the initial state which undergoes the transition to the end state is denoted by $N_{v',J'}$; $A_{(v',J' \to v'',J'')}$ is the Einstein coefficient of

this specific spontaneous emission (in s^{-1}), which describes the transition probability. If LTE holds for the rotational populations, the distribution of the molecules over the different rotational quantum numbers follows the Boltzmann distribution:

$$N_{v',J'} = \frac{N_{v'}}{Q_{v'}(T)} (2J'+1) \exp\left(-\frac{E_{v',J'}}{k_B T_{rot}}\right), \quad (8)$$

where $N_{v'}$ is the total number of molecules in the vibrational level v' and $Q_{v'}(T)$ is the partition function or state sum defined (Thorne, 1988):

$$Q_{v'}(T) = \sum_{J'} (2J'+1) \exp\left(-\frac{E_{v',J'}}{k T_{rot}}\right), \quad (9)$$

which is a function of temperature.

The factor $(2J'+1)$ is due to the degeneracy of the state; $E_{v',J'}$ is the upper-state rotational energy, k_B the Boltzmann constant, and T_{rot} the rotational temperature, which is equal to the kinetic temperature for LTE. Substitution of $N_{v',J'}$ in Eq. (7) according to Eq. (8) gives the following:

$$I_{(v',J' \to v'',J'')} = \frac{N_{v'}}{Q_{v'}} (2J'+1) \exp\left(-\frac{E_{v',J'}}{k_B T_{rot}}\right)$$
$$\cdot A_{(v',J' \to v'',J'')}. \quad (10)$$

So, the intensity of the lines of a rotational–vibrational transition depends non-linearly on the rotational temperature.

Equation (10) can be reformulated as follows:

$$\underbrace{\ln\left(\frac{I_{(v',J'\to v'',J'')}}{A_{(v',J'\to v'',J'')}\cdot(2J'+1)}\right) - \ln\left(\frac{N_{v'}}{Q_{v'}}\right)}_{=:b}$$

$$\underbrace{-\frac{1}{k_B T_{rot}}}_{=:m}\cdot E_{v',J'} = 0. \tag{11}$$

Equation (11) now describes a linear relation, i.e. a straight line with b as the y-axis intercept and the line slope m. The term $\frac{I_{(v',J'\to v'',J'')}}{A_{(v',J'\to v'',J'')}\cdot(2J'+1)}$ is partly known – even though there is some discussion about the true value of the Einstein coefficient (see Noll et al., 2020 and references therein, and Tables 2.4–2.13 in Khomich et al., 2008 for an overview of some of them) – and can partly be taken directly from the airglow measurement. While $\frac{N_{v'}}{Q_{v'}}$ is not known but constant, $E_{v',J'}$ is known. Measuring the OH* airglow intensity for at least two different rotational transitions of one vibrational branch and plotting the intensity versus $E_{v',J'}$ allows fitting a line with a slope determined by the inverse of the rotational temperature and the Boltzmann constant. The advanced mesospheric temperature mapper (Pautet et al., 2014 and references therein) is an example of an instrument where only a pair of lines ($P_1(2)$ and $P_1(4)$ of OH(3-1) band) are used. In many cases, three or more rotational lines are used, which makes the fit more robust, and provides an immediate measure of the uncertainty of the temperature retrieved (e.g. French et al., 2000; Sigernes et al., 2003). Based on astronomical sky spectra, Cosby and Slanger (2007) and Noll et al. (2017), for example, showed that retrieved temperatures T_{rot} depend on the vibrational level v'. There is the overall trend that higher vibrational levels lead to higher temperatures (non-LTE effect), even though there is some variation with the vibrational level. This observation is justified by the thermal equilibration efficiency of collisions which is altitude-dependent (and therefore v'-dependent). Vibrational transitions with $\Delta v = 1$ are the brightest (see Fig. 4.6 from Roach and Gordon, 1973, or Krassovsky et al., 1962, p. 900). From the ground, only bands with $\Delta v \geq 2$ can be detected, which means that the emitted wavelength is shorter or equal to 2.1 µm (Khomich et al., 2008). Ground-based OH* airglow spectrometers in many cases use the OH(3-1) or OH(4-2) transitions in the wavelength region 1.5–1.6 µm, where atmospheric absorption is minimized (see e.g. Bellisario et al., 2020; also Chadney et al., 2017, and Espy and Hammond, 1995). The P branch of these bands is preferred since the energy difference between the different rotational transitions increases with increasing rotational quantum number. Therefore, the free spectral range (the distance between two lines in the spectrum) is larger than for the Q and R branches.

Once the temperature has been determined from a number of lines within a band, the intercept in Eq. (11) allows a value of $ln\left(\frac{N_{v'}}{Q_{v'}}\right)$ to be calculated. Knowledge of the behaviour of $Q_{v'}(T)$ as a function of temperature (Krassovsky et al., 1962) then provides a method of calculating $N_{v'}$, the number of OH* in the upper vibration state of the band under study. The total intensity of the band can then be determined (Hecht et al., 1987) from

$$I_{v'\to v''} = N_{v'}A_{v'\to v''}, \tag{12}$$

where $A_{v'\to v''}$ is the Boltzmann-averaged Einstein coefficient. This latter value is independent of temperature over the range of values obtained in the altitude range of the OH* layer.

While the method of calculating band intensity values just described is straightforward, the majority of intensity measurements reported are however relative values. For a given instrument, relative intensity values are suitable for many studies, and it avoids the need to address the difficult twin problems of intensity calibration of instruments and taking account of atmospheric extinction. Unfortunately, the use of relative intensity values makes it impossible to compare results from different instruments. This makes the relatively few reports of intensity values (e.g. Harrison and Kendall, 1973; Sivjee and Hamwey, 1987; Hecht et al., 1987; Mulligan et al., 1995; Espy and Stegman, 2002) all the more valuable. Comparison of results from ground-based instruments with VER measurements from satellite instruments such as SABER on TIMED provides a way for ground-based observers to obtain approximate values for their intensity values, and thereby compare their results with other observers.

Since the first observation of OH* airglow, the technique improved according to the developments in instrumentation detector materials (higher spectral resolution and/or increased signal-to-noise ratio, SNR), and in digitalization, but also the determination of parameters needed for the temperature retrieval (e.g. Einstein coefficients) have evolved since then. Photo plates were replaced by single-cell Germanium (Ge) detectors (Shemansky and Jones, 1961) and then by further materials such as Gallium Arsenide (GaAs) or Indium Gallium Arsenide (InGaAs) (e.g. see Misawa and Takeuchi, 1977, 1978: OH(8-3) around 727 nm, InGa photomultiplier; Scheer, 1987: airglow between 845–867 nm, GaAs photomultiplier; Mulligan et al., 1995: airglow at 1–1.65 µm, single-cell InGaAs detector; Greet et al., 1998: airglow 800–900 nm, GaAs photomultiplier; Suzuki et al., 2008: airglow at 800–1700 nm, InGaAs detector array; Schmidt et al., 2013: airglow at 1.5–1.6 µm, InGaAs detector array). The SNR is worse for InGaAs compared to the Ge detector operated in the 1980s and 1990s, e.g. by Bittner et al. (2000); however, since the noise is relatively constant with time and regularly determined during a dark current measurement, this disadvantage could be overcome. While the Ge detector used by Bittner et al. (2000) needed liquid nitrogen cooling for a good SNR, InGaAs detectors deliver spectra at higher detector temperatures, which can be achieved by thermoelectric cooling, which is much more practical than the use of liquid nitrogen. The elimination of liquid nitrogen cooling

facilitates unattended operation. Line detectors or linear detector arrays (Schmidt et al., 2013) allow the simultaneous measurement of a larger spectral range and avoid scanning mechanisms. This improves the temporal resolution of OH* airglow spectrometer measurements by an order of magnitude, from some minutes to ca. 10 s, and enables us to address the infrasound spectrum (Pilger et al., 2013), at least in parts. The automation of the temperature retrieval from the spectra allows the rapid analysis of spectra.

A new development published by the University of Wuppertal is the spatial heterodyne interferometer GRIPS-HI, which is a hybrid combining properties of both grating spectrometers and Fourier interferometers (Stehr et al., 2021). It is sensitive to 1520–1550 nm. Its advantage over grating spectrometers is the spectral resolution and the optical throughput, which are regarded as main sources of measurement uncertainty. Furthermore, temperature measurements can be resolved spatially in 1D, even when the instrument is not scanning (Harlander et al., 2002). However, until now, only a prototype of GRIPS-HI exists, which still needs some improvement.

When using an airglow spectrometer based on a single detector cell or a line detector, the OH* airglow signal is averaged horizontally over the FoV. The size of the sensed area at OH* layer altitude depends on the optics of the spectrometer but also on the zenith angle at which the instrument is operated. This needs to be taken into account when interpreting the results, especially with respect to gravity wave parameters. The influence of different zenith angles on the sensitivity of an OH* airglow spectrometer for gravity waves is shown in Wüst et al. (2016), e.g. (in the context of satellite validation, the reduced sensitivity to spatial features due to the non-infinitesimally small sensed air volume is known as observational filter). With airglow spectrometers based on a single detector cell or a line detector, horizontal wave parameters cannot be derived straight away – camera systems would be required for this.

Different from OH* airglow spectrometers, the values of OH* cameras are not averaged over the whole FoV, their spatial resolution depends on the number of pixels on the chip, the objective used, and the zenith angle of the instrument. Effects of spatial resolution need to be considered when results of different instruments are compared. When using OH* airglow cameras with suitable filter wheels which are sensitive to different rotational transitions of one vibrational band, temperature information can be retrieved (without scanning the night sky) as done by Pautet et al. (2014); also SATI provides a temperature image but with a worse spatial resolution than Pautet et al. (2014), covering 12 different azimuth angles of the observed annulus in the airglow layer (López-González et al., 2007). Technical developments have made the imaging systems smaller and the instruments more compact, so that they are relatively easy to deploy on aircraft, for example. The history of imaging wave structures in the OH* layer until the late 1990s is reviewed in Taylor (1997).

4 Results from OH* airglow measurements

A large number of publications are available on the topic of analysing OH* airglow data measured from ground, starting with Krassovsky (1972). The FoV as well as the spatial and temporal resolutions of an instrument limit the range of dynamic phenomena that can be observed. For example, the temporal resolution of most instruments is not well-suited for infrasound observations, and in the case of imaging systems, the spatial resolution does not allow the display of planetary waves. However, planetary waves can be addressed in the temporal domain by spectrometers and cameras, and therefore individual OH* airglow measurements allow the observation of travelling planetary waves or show the superposition of stationary and travelling planetary waves. Generally, it is not necessary to derive the rotational temperature for the analysis of gravity waves based on OH* measurements. As mentioned earlier, wave-induced fluctuations in intensity are larger than in temperature and smaller vertical wavelengths can be derived from intensity time series compared to rotational temperature time series. However, for the derivation of some gravity wave parameters, knowledge about the wave-induced temperature perturbation is needed.

The advantage of ground-based OH* airglow observations is that some of them have been made over many years. This allows the investigation of the long-term temperature development or long-term analyses of gravity wave parameters, for example. The results of some publications with the longest time series focussing on gravity waves (or dynamics) are summarized in the following section.

Concerning airborne results, the number of publications is limited as OH* airglow instruments are not a suitable equipment for commercial aircraft (such as CARIBIC for the troposphere). They need special ports in the upper part of the aircraft through which they can receive incoming light and which incur high-cost and licence issues amongst others. Therefore, they are only operated on research aircraft on a campaign basis. Some of the campaigns reported in the literature, e.g. EXL98 (Energetics of Upper Atmospheric Excitation by Lightning in 1998), Leonid MAC, ALOHA-90 and -93, DEEPWAVE (Deep Propagating Gravity Wave Experiment), and GW-LCYCLE (Gravity Wave Life CYCLE), are addressed in the following sections.

Analyses of OH* airglow spectroscopy time series directly deliver gravity wave periods and their amplitudes in intensity and temperature. The respective parameters are subject to vertical, horizontal, and temporal averaging. For most scientific questions, the temporal averaging is negligible (the temporal resolution is mostly in the range of seconds to minutes). OH* airglow imagery additionally allows the extraction of horizontal wavelengths of gravity waves, their horizontal phase velocities, and of their horizontal propagation direction. Spatial scanning spectrometers are able to do the same (Wachter et al., 2015; Wüst et al., 2018), however, their sensitivity to horizontal structures is limited since a scan-

ning spectrometer is always a compromise between the time needed for the scan, the size of the scanned region, and the size of the individual FoV.

Based on the dispersion relation for gravity waves or its simplifications according to the observed period range, further wave parameters such as the vertical wavelength of gravity waves can be calculated (e.g. Swenson and Liu, 1998; Suzuki et al., 2007 for imaging systems; Wüst et al., 2018 for a scanning spectrometer):

$$m^2 = \frac{(k^2 + l^2)(N^2 + \hat{\omega}^2)}{\hat{\omega}^2 - f^2} - \frac{1}{4H^2}, \tag{13}$$

where k, l, m denote the zonal, meridional, and vertical wave number, respectively; N is the Brunt–Väisälä frequency; f is the Coriolis frequency; $\hat{\omega}$ is the intrinsic GW frequency ($\hat{\omega} = \omega - u \cdot k - v \cdot l$ where u and v are the zonal and meridional background wind velocities, respectively, and ω is the GW frequency); and H is the scale height.

However, for the application of the dispersion relation, additional information such as the Brunt–Väisälä frequency and wind velocities is mandatory.

Based on OH* airglow transitions, horizontal wind velocities can be measured using Fabry–Perot interferometers (e.g. Shiokawa et al., 2001). However, as far as we know, the data do not allow the derivation of gravity-wave-induced fluctuations due to relatively large uncertainties, which limits its use for the calculation of kinetic GW energy, for example. A better time resolution and lower uncertainties may be possible with Michelson interferometers such as ERWIN (Gault et al., 1996) and ERWIN II (Kristoffersen et al., 2013). They also allow 2D imaging of line-of-sight winds (Langille et al., 2013). Alternative non-airglow wind measurement techniques such as lidar or radar achieve a temporal resolution in the range of 1 h or less (e.g. Rauthe et al., 2006; Jacobi et al., 2009).

The Brunt–Väisälä frequency cannot be taken from OH* airglow measurements; it can at best be estimated, especially during summer when the OH* layer is in the range of a small vertical temperature gradient. Therefore, coincident lidar (Tang et al., 2002) or satellite measurements of the vertical temperature profile or climatologies of the Brunt–Väisälä frequency (e.g. Wüst et al., 2017, 2020) are necessary. Then, the density of gravity wave potential energy (GWPED) can be calculated when the rotational temperature measurements are separated into wave-induced temperature variations and background temperature. Based on the amount of potential energy, kinetic energy can at least be estimated – from linear gravity wave theory, the ratio of kinetic (mostly horizontal) to potential energy is predicted to be equal to ca. 5/3 (Van Zandt, 1985). In order to quantify gravity wave activity without providing kinetic or potential energy (density), the variability of the data in terms of standard deviation or based on spectral analyses is provided by some authors (e.g. Offermann et al., 2009, López-González et al., 2020, and citations therein). Since the majority of imaging systems are not able

to derive temperature, the GWPED is in most cases only calculated from spectrometer measurements.

An alternative way to derive the vertical wavelength of GW without information about the horizontal wind is the measurement of different vibrational transitions (Schmidt et al., 2018) since their respective centroid heights differ by ca. 500 m for adjacent upper vibrational levels (see Fig. 1b, right panel). Furthermore, the fact that the signal of maximal temperature variations originates from a height other than the signal of maximal intensity variation (the height of the maximum intensity perturbation is lower than the height of the maximum temperature perturbation) can be used (Reisin and Scheer, 2001). This leads to a phase shift ϕ when the wave is derived from rotational temperature and intensity time series and this phase shift is related to the vertical wavelength λ_z:

$$\phi = \frac{I_s}{\lambda_z} 360°, \tag{14}$$

where I_s is the effective layer separation (which was given by ca. 3.75 km according to Swenson and Gardner, 1998 for their model setup). Since the effective layer separation can vary, this method at least gives an estimate for the vertical wavelength. As already mentioned earlier, the sensitivity of intensity and temperature to small vertical wavelengths is limited by the integration of the variation through the OH* layer profile (typically ~ 8 km). This limits the application of Eq. (14).

If the vertical and horizontal wavelengths, λ_z and λ_h, are known, momentum and energy flux, F_M and F_E, can be estimated from the volume integrated OH* intensity based on the so-called cancellation factor (CF), which is determined by the ratio of the relative intensity and the relative atmospheric temperature (relative in the sense of wave-disturbed value divided by undisturbed value, Swenson and Liu, 1998; Suzuki et al., 2007) with

$$F_M = \frac{6 \cdot 10^4 \cdot \lambda_z \cdot (I'_{OH})^2}{\lambda_h \cdot CF^2 \cdot (I_{OH})^2}, \tag{15}$$

and

$$F_E = \frac{2.3 \cdot 10^{-3} \cdot \lambda_z^2 \cdot (I'_{OH})^2}{\lambda_h \cdot CF^2 \cdot (I_{OH})^2}, \tag{16}$$

where I'_{OH} is the wave-perturbed volume integrated OH* intensity and I_{OH} the unperturbed one.

These quantities are only conserved in the absence of a background wind; in the presence of a background wind, pseudo-energy and pseudo-momentum are conserved (Nappo, 2013). (Pseudo-)energy or momentum conservation only holds if no energy or momentum dissipation takes place.

4.1 Ground-based measurements

For review, we select a number of OH* airglow atmospheric wave studies utilizing observations from a number of stations

or which show long-term results from a comprehensive range of ground-based OH* airglow research.

Starting with planetary waves, Reisin et al. (2014) used rotational temperatures measured at 19 sites from 78° N to 76° S to derive monthly and total mean climatologies of planetary wave activity. All of these sites belong to the Network for the Detection of Mesospheric Change (NDMC). Most sites between 69° S and 69° N show similar planetary wave activity; it is only at some high-latitude sites that relatively high activity is observed. At all high-latitude sites, the seasonal variability is relatively high compared to 70 % of the mid-latitude stations and the two tropical stations, which show practically no seasonal variation of PW activity.

Based on 12 years of OH* airglow spectrometer measurements at Wuppertal (51° N, 7° E), Germany, and complementary satellite measurements, Offermann et al. (2009) investigated the influence of planetary and gravity waves as well as tides as sources of fluctuations on vertical temperature profiles in the UMLT. They showed that gravity waves are responsible for the majority of those fluctuations. Travelling planetary waves are more important in this context than quasi-stationary ones. The strength of tidal fluctuations lies within the range of travelling planetary wave fluctuations or below it, depending on latitude (the higher the latitude the lower the tidal strength).

It can be a challenge to separate gravity waves and tides in OH* airglow measurements since gravity waves can have periods in the range of the semi-diurnal tide, for example, and large-scale spatial information is often not available, which would help to distinguish the different wave types. Another possibility to separate gravity waves and at least migrating tides is to search for signals with phases (e.g. see Fig. 6 of Silber et al., 2017) and periods typical for tides over some consecutive nights. However, data availability has to allow for this procedure. For the extraction of tides based on a spectral analysis, for example, it is worth noting that tidal amplitudes can change within a few days (Silber et al., 2017). Probably due to these reasons, OH* airglow studies of atmospheric tides (relying on time series of some years or a network of instruments) are not common. One example based on measurements at the Sierra Nevada Observatory (37.06° N, 3.38° W) in the time period of 1998–2003 is given by López-González et al. (2005), who analysed the data with respect to diurnal variations. Emission rates and rotational temperatures both show diurnal tidal signals with seasonal variation (greater from late autumn to spring than during summer).

Recently, López-González et al. (2020) analysed OH* airglow measurements at the same observatory from 1998 to 2015 with respect to gravity waves. Gravity wave activity with periods shorter than 3 h shows a maximum in summer and winter. Gravity waves with periods from 3 to 6 h have maximum activity around October–December and a minimum during summer. These cycles can also be observed in the GWPED, which was derived by Wüst et al. (2016) with five technically identical OH* airglow spectrometers from 2011 to 2014 at four NDMC stations (three stations in central and one in Northern Europe). Due to the instrument sensitivity, those authors split the results into periods longer and shorter than 60 min. Based on multi-year measurements at eight different, mostly European stations, Sedlak et al. (2020) showed that a gradual transition in gravity wave activity exists from a semi-annual cycle with a slight primary maximum in summer for very short periods (60 min and less) over a semi-annual cycle with two maxima of equal strength in summer and winter to an annual cycle with a maximum in winter for periods of ca. 400 min.

Vargas et al. (2015) examined gravity wave propagation directions from OH* airglow imager measurements at more than 20 different stations including those with only a few clear measurement nights up to those that had as many as 513 clear measurement nights in a time period of up to 7 years. While the stations are distributed all over the world, the longitudinal sector of ca. 25° W to 75° E is covered by only one station (Esrange, Sweden), which due to its high-latitude position (68° N), provided data only during the northern winter. The preferential propagation direction of high-frequency gravity waves is toward the summer pole and to the east (west) during summer (winter). While the zonal propagation direction is consistent with the assumption of stratospheric wind filtering, there is some inconsistency about the meridional propagation direction. This picture does not change in more recent literature which focuses on two stations in central Europe (Oberpfaffenhofen, Germany, 48.09° N, 11.28° E, and Sonnblick, Austria, 47.05° N, 12.96° E; Hannawald et al., 2019). Local variations are superimposed on the preferred propagation directions from these stations.

Rourke et al. (2017) analysed data from a scanning radiometer between 1999 and 2013 and looked for the height of origin of gravity waves. The instrument deployed at Davis Station, Antarctica (68.6° S, 78.0° E) is sensitive to radiation in the range of 1.10–1.65 μm and covers a small region (24 × 24 km) of the zenith night sky once per minute. The authors found that on average, only 15 % of the detected gravity waves can be reverse ray-traced to the troposphere. Most of the end points were found within a radius of 300 km of the station. Approximately 45 % were not successfully traced back substantially below the airglow layer.

In a similar fashion to tides, infrasound and turbulence are not often studied using OH* airglow measurements. In the case of infrasound, Le Dû et al. (2020) identified infrasound signals in the frequency band of those produced by ocean swell in OH* imager data at the Haute-Provence Observatory, France. Inchin et al. (2020) modelled infrasonic waves generated by an analogue of the 2011 M9.1 Tohoku-Oki earthquake. Those authors found out that these waves may be strong enough to drive fluctuations in the UMLT airglow, which could be detectable with ground- and/or satellite-based imagers. Pilger et al. (2013b) presented examples for airglow measurements of orographic, volcanic, and meteorological infrasound signatures based on spectrometer data.

The only publication in this context that is based on a larger amount of data is the one by Pilger et al. (2013a), who used 40 months of spectrometer data and found evidence for acoustic resonance modes.

The investigation of turbulence in OH* airglow measurements is in most cases based on the observation of so-called ripples (see e.g. Hannawald et al., 2016; Sedlak et al., 2016). Ripples are wave-like structures with horizontal wavelengths of 5–15 km (Li et al., 2005; Taylor et al., 1995) or 20 km at most (Takahashi et al., 1985). They have a short lifetime of 45 min or less with periods close to 5 min (Hecht, 2004) and are often interpreted as manifestations of Kelvin–Helmholtz instabilities (dynamical instabilities) or convective instabilities. However, based on OH* all-sky imager measurements at Yucca Ridge Field Station, Colorado (40.7° N, 104.9° W), from September 2003 to December 2005 and additional measurements, Li et al. (2017) showed that more than half of the observed ripples might not be instability features but wave structures that are hard to distinguish from real instability features. In this case, the ripples could be related to secondarily generated small-scale gravity waves (Vadas et al., 2003; Zhou et al., 2002). Another possibility to analyse turbulence is the observation of vortices as Sedlak et al. (2016) and Hecht et al. (2021) showed based on case studies of an imager system with a very high spatial resolution of 17 and 25 m per pixel, respectively. In their more recent work, Sedlak et al. (2021) extended their study to 1.5 years of data which include some 20 to 30 case studies. With an instrument originally set up for astronomical observations (NOTCam spectrograph mounted on the Nordic Optical Telescope (NOT) in La Palma), Franzen et al. (2018) found quasi-periodic structures with minimal horizontal wavelengths of 4.5 m following a Kolmogorov-type energy cascade during breaking.

4.2 Airborne measurements

The number of airborne OH* airglow measurements is generally relatively small. To our knowledge, the first airborne measurement was performed by Noxon (1964) during a single night from a jet aircraft flying at 75° W longitude from 55 to 85° N. The author analysed the dependence of the rotational temperature and the intensity on latitude. Concerning GW, there are only five larger campaigns reported during which such measurements were performed to our knowledge – three between 1993 and 1999 and two between 2014 and 2016.

Anderson et al. (2008) used an aircraft-mounted spectroscopic imager to tomographically reconstruct atmospheric gravity waves, i.e. to estimate the horizontal–vertical airglow structure. The authors illustrate the applicability of their algorithm based on data taken during the ALOHA campaign, which took place in October 1993. During the same campaign, Swenson and Espy (1995) investigated imager measurements of gravity waves in the vicinity of a tropospheric low pressure system. Due to cloud formation, this was not possible in most cases or possible only at large zenith angles (which directly affect the FoV and therefore the spatial resolution) for ground-based instruments.

Siefring et al. (2010), amongst others, used an airborne camera (900 to 1700 nm) to observe sprites but also airglow during the EXL98 campaign. Gravity wave activity and therefore density variations were investigated by the authors. Ionization rates are highly dependent on the neutral density and hence gravity waves may have an effect on the location and filamentation of sprites, causing brightness variations in elves. Such a correlation was observed in one case.

During the Leonid MAC Campaign, airglow spectra and imaging data of airborne instruments were used to study upper atmospheric conditions. The temporal focus was on a period centred on the Leonid meteor storm of 17–18 November, 1999 as well as on the meteor storm itself. Kristl et al. (2000) found a small but significant enhancement in the OH* airglow emission during the peak of the storm. However, the authors admit that they are not certain of the cause.

During the DEEPWAVE campaign project over New Zealand and surrounding regions, a strong gravity wave event was observed by Pautet et al. (2019) during June and July 2014 using three airborne OH* airglow imagers. It remained at the same location for at least 4 h, had a dominant horizontal wavelength of ca. 40 km, and together with additional measurements, its momentum flux per unit mass was estimated to be at least $320\,\mathrm{m}^{-2}\,\mathrm{s}^{-2}$. The authors associated these waves with orographic forcing generated by moderate surface flow over a small island terrain.

In January and February 2016, an airborne OH* airglow camera was measured during the GW-LCYCLE campaign in Northern Europe. Two of six flights were analysed by Wüst et al. (2019) with respect to gravity waves with horizontal waves between 3 and 26 km. The results were separated for waves shorter and longer than 15 km (bands and ripples). The most mountainous regions were characterized by the highest occurrence rate of wave-like structures – in one flight due to ripples, in one flight due to bands. At least for one flight, the propagation of mountain waves was not possible or at least strongly reduced.

4.3 Satellite-based measurements

Ground-based and airborne instruments are usually not able to provide information about the height of the OH* airglow layer. The first investigations of the OH* emission height (and in some instances the FWHM of the OH* layer) were performed on a case study basis some 35–45 years ago, mostly relying on rocket-borne or lidar measurements (Good, 1976; Von Zahn et al., 1987; Baker and Stair, 1988 and citations therein).

With the launch of WINDII (Wind Imaging Interferometer; Shepherd et al., 1993) on board UARS (Upper Atmosphere Research Satellite) in September 1991, decadal satellite-based and therefore near-global limb investigations

of the OH* airglow emissions were possible. The WINDII was followed by OSIRIS (Llewellyn et al., 2004) on board Odin, SCIAMACHY (Scanning Imaging Absorption Spectrometer for Atmospheric Chartography; Bovensmann et al., 2004), and GOMOS (Global Ozone Monitoring by Occultation of Stars; Kyrölä et al., 2004) on board ENVISAT (ENVIronmental SATellite, January 2003–December 2011), SABER (Russell III et al., 1999) on board TIMED (ongoing since December 2001), ISUAL (Imager of Sprites and Upper Atmospheric Lightnings; Rajesh et al., 2009) on board Formosat 2, and MLS (Waters et al., 2006) on board EOS-Aura. Details about the measurement parameters and the hemispheric coverage are shown in Table 1.

Satellite measurements can serve as complementary measurements for ground-based and airborne ones. A very nice example of the benefits that can be derived by combining ground- and satellite-based measurements is illustrated in Shepherd et al. (2020). The scale of the event chosen for study makes good use of the longitudinal separation of the ground stations. The two ground-based datasets were augmented with temperature profiles from the MLS instrument on the Aura satellite, which enabled the investigators to obtain an overall picture of the state of the atmosphere in the polar cap before, during, and after the occurrence of a sudden stratospheric warming (SSW), which had some unusual features. The report illustrates the benefits of using multiple datasets in elucidating different aspects of this complex natural phenomenon. While the satellite data provide a global overview of the event, the ground-based observations of both temperature and wind allowed the event to be probed with high temporal resolution.

Long-term satellite measurements provide information about the OH* airglow layer characteristics and their development (e.g. von Savigny, 2015 and Wüst et al., 2017). As mentioned in Sect. 2, height, thickness, and brightness of the OH* airglow layer are linked. The relationship between the column-integrated volume emission rate and the peak emission height as it is derived from satellite-based measurements can be used, for example, to infer the OH* layer height from ground-based measurements alone (e.g., Liu and Shepherd, 2006; Mulligan et al., 2009).

Satellite-based measurements are also valuable for temperature comparisons with ground-based sites (e.g. López-González et al., 2007) and temperature trend analyses over global scales. For example, French et al. (2020) combined ground- and satellite-based measurements to assess temperature trends. They derived a long-term cooling trend of $-1.2 \pm 0.51\,\mathrm{K}$ per decade based on 24 years of measurements at Davis Station, Antarctica. In their Table 1, they also provide trend estimates based on further OH* airglow measurement stations from the literature, which are all negative. Additional analyses of 14 years of near-global Aura/MLS data show that the temperature trends at the hydroxyl-layer-equivalent pressure level are significantly non-uniform across the globe and that positive trends can be observed in some regions.

Further satellite-based OH* airglow instruments, which should be mentioned in this context are nadir-looking ones such as VIRRS DNB (Day/Night Band nightglow imagery from the Visible/Infrared Imaging Radiometer Suite) on board Suomi NPP (Suomi National Polar orbiting Partnership, ongoing since October 2011) and JPSS-1 (Joint Polar Satellite System-1). They do not provide additional information about the OH* layer height or thickness such as limb-viewing systems; however, they allow for the analysis of horizontal GW parameters with a spatial resolution of ca. 0.75 km on moonless nights, independent of the weather conditions (see Miller et al., 2015 and Yue et al., 2019 and references mentioned therein). This is of great advantage for the observation of gravity waves generated by convective systems (e.g. Miller et al., 2012; Xu et al., 2019; Yue et al., 2014), which is limited from the ground due to cloud coverage. The use of nadir measurements is not restricted to this purpose, but includes other possible GW sources such as orography or seismic and volcanic events that are investigated (Miller et al., 2015). This is done in case studies. Long-term studies relying on VIRRS DNB are yet to be published to our knowledge.

5 Summary and outlook

Ground-based OH* airglow measurements have been carried out for almost 100 years. At some sites, they are available for decades. Advanced detector technology has greatly simplified the automatic operation of OH* airglow observing instruments and significantly improved the temporal and, in the case of imagers, the spatial resolution of these measurements. Studies based on long-term measurements (i.e. 10 years or more) or including a network of instruments have been reviewed, especially in the context of deriving gravity wave properties.

The parameters investigated include periods or horizontal wavelengths, which always depend on the technical specifications and the measurement geometry of the instruments. In addition, wave propagation direction and activity (which is defined differently in many studies) or density of potential energy are derived. To a large extent, today's challenges lie in the field of analyses. Improved temporal and spatial resolution reduce averaging effects in space and time, therefore, more non-stationary processes become evident in the data. Additionally, the amount of data increases.

Information about the wind at the OH* airglow layer height allow the computation of additional wave parameters. Wind data based on the OH* airglow can be measured with Fabry–Perot or Michelson interferometers. However, those measurements are not quite frequent.

Ray tracing studies for source attribution of waves measured through OH* airglow observations and whether these waves are primary ones (so generated directly by convection or flow over mountains, for example) or result from possi-

Table 1. Summarized are the different satellite-based instruments which deliver information about OH* and some additional information about satellite launch date, data availability, observed OH* transition and if available, additional temperature and/or wind measurements from the instrument, which might be useful in the context of atmospheric dynamics. Data are available some time after the launch date depending on the duration of test phases of the satellite and the instruments.

Instrument	Satellite	Launch date	Data until	Latitudinal range	OH* transition	Additional notes	References
WINDII Wind imaging interferometer	UARS Upper atmosphere research satellite	12 September 1991	2003	42° in one hemisphere to 72° in the other one, alternating every 36 d	OH(8-3)	Wind, temperature available	Shepherd et al. (1993, 2012)
OSIRIS Optical spectrograph and infrared imager system	Odin	20 February 2001	Ongoing	Ca. one hemisphere up to 82° S/N at maximum, alternating every 6 months	OH(8-3), OH(9-4), OH(5-1), OH(3-1)		Llewellyn et al. (2003, 2004); Sheese et al. (2014) https://research-groups.usask.ca/osiris/ (last access: 28 June 2021)
SABER Sounding of the atmosphere using broadband emission radiometry	TIMED Thermosphere ionosphere meso-sphere energetics dynamics	7 December 2001	Ongoing	52° in one hemisphere to 83° in the other one, alternating every 60 d	OH VER @1.6 and 2.1 µm, OH(v = 3, 4, 5) & OH(v = 7, 8, 9)	Temperature available (derived from CO_2)	Russell III et al. (1999)
SCIAMACHY SCanning Imaging Absorption spectroMeter for Atmospheric CHartographY	ENVISAT Environmental satellite	1 March 2002	8 April 2012	35° S–65° N, seasonal variation	OH(3-1), OH(8-3), OH(6-2)	Temperature available	von Savigny (2015, 2004, 2012)
GOMOS Global ozone monitoring by occultation of stars				70° S–70° N, seasonal variation	OH(8-4)		Bellisario et al. (2014); Chen et al. (2019)
ISUAL Imager of sprites and upper atmospheric lightnings	Formosat 2	20 May 2004	2016	Only for 2 orbits each day, addressed lat. range varies, in northern summer ca. 30° N	OH(9-3)		Rajesh et al. (2009); Nee et al. (2010); https://directory.eoportal.org/web/eoportal/satellite-missions/f/formosat-2 (last access: 28 June 2021)
MLS Microwave limb sounder	EOS-Aura Earth observing system, aura = Latin for breeze	15 July 2004	Ongoing for 30 d measurement each year since 2011 Stop of continuous measurement 2009	82° S–82° N	OH @ ca. 2.5 THz (120 µm)	Temperature available (derived near O_2 band)	Waters et al. (2006); https://mls.jpl.nasa.gov/eos-aura-mls/data-products/oh (last access: 28 June 2022)

ble wave–wave or wave–mean flow interactions are rare. For this, additional information, e.g. on the state of the atmosphere (especially temperature, wind) at other altitudes are needed. Wave propagation models can provide further information, if the corresponding processes are included. For the analysis of non-linear wave–wave interactions, comprehensive information about the parameters of the different waves are needed (e.g. see Wüst and Bittner, 2006).

The horizontal resolution of ca. 10–20 m, which is achieved today in the best case by OH* airglow imagers, makes it possible to observe turbulence eddies and to estimate the energy emitted by gravity waves and thus the heating rates of the atmosphere by gravity waves. However, for the analysis of larger datasets, the automatic detection of these vortices is necessary. This requires the use of analysis methods other than those applied so far. Here, first steps are currently being taken in the field of artificial intelligence and machine learning. For example, Lai et al. (2019) showed how to identify cloudless nights in all-sky OH* airglow imager time series and how to locate the wave patterns in each picture.

The observation of infrasound with the help of OH* airglow measurements is currently still quite difficult. Especially in the context of observing and learning more about natural hazards (Bittner et al., 2010), the detection of infrasound is of interest as Inchin et al. (2020) modelled. Here, OH* airglow intensity measurements are better suited than temperature observations.

Clouds generally hinder the ground-based detection of OH* airglow emissions, sunlight significantly reduces the detected airglow intensity. For other species such as oxygen airglow (green line: 557.7 nm centred at night around a height of 97 ± 3 km (Wolff, 1966), red line: 630 nm centred around 300 km (Danilov, 1962), which is relatively broad compared to the other airglow layers mentioned here), it could be shown that ground-based daytime measurements are possible based on different instruments (see Marshall et al., 2011; Pallamraju et al., 2002 and citations therein). For OH* airglow, at least to our knowledge, only one technique is published using a multiwavelength photometer (Sridharan et al., 1998). The OH* dayglow shows a double-peak structure: the upper layer is located at a similar altitude as in the case of OH* nightglow, the lower layer is between 70 and 85 km in height, increasing with time of the day (Gao et al., 2015). Additionally, the proportion of scattered light is relatively high during the day, so that very narrow-band filters are necessary, which reduces the light yield and decreases the temporal resolution. Daytime measurements of OH* airglow therefore do not allow a comparable continuation of nocturnal measurements.

References

Adler-Golden, S.: Kinetic parameters for OH nightglow modeling consistent with recent laboratory measurements, J. Geophys. Res.-Space, 102, 19969–19976, https://doi.org/10.1029/97ja01622, 1997.

Anderson, D. S., Swenson, G., Kamalabadi, F., and Liu, A.: Tomographic imaging of airglow from airborne spectroscopic measurements, Appl. Opt., 47, 2510–2519, https://doi.org/10.1364/ao.47.002510, 2008.

Andrews, D. G.: An introduction to atmospheric physics, 3rd Edition, Cambridge University Press, ISBN 0521629586, 2000.

Baker, D. J.: Studies of atmospheric infrared emissions, Utah State University, Logan Electro-Dynamics Lab, https://apps.dtic.mil/sti/pdfs/ADA072831.pdf (last access: 6 December 2022), 1978.

Baker, D. J. and Stair, A. T.: Rocket measurements of the altitude distributions of the hydroxyl airglow, Physica Scripta, 37, 611–622, https://doi.org/10.1088/0031-8949/37/4/021, 1988.

Baker, D. J., Steed, A. J., Ware, G. A., Offermann, D., Lange, G., and Lauche, H.: Ground-based atmospheric infrared and visible emission measurements, J. Atmos. Terr. Phys., 47, 133–145, https://doi.org/10.1016/0021-9169(85)90129-1, 1985.

Bates, D. R. and Nicolet, M.: The photochemistry of atmospheric water vapor, J. Geophys. Res., 55, 301–327, 1950.

Battaner, E. and Lopez-Moreno, J. J.: Time and altitude variations of vibrationally excited-states of atmospheric hydroxyl, Planet. Space Sci., 27, 1421–1428, https://doi.org/10.1016/0032-0633(79)90088-6, 1979.

Becker, E., Grygalashvyly, M., and Sonnemann, G. R.: Gravity wave mixing effects on the OH*-layer, Adv. Space Res., 65, 175–188, https://doi.org/10.1016/j.asr.2019.09.043, 2020.

Bellisario, C., Keckhut, P., Blanot, L., Hauchecorne, A., and Simoneau, P.: O_2 and OH Night Airglow Emission Derived from GOMOS-Envisat Instrument, J. Atmos. Ocean. Tech., 31, 1301–1311, https://doi.org/10.1175/jtech-d-13-00135.1, 2014.

Bellisario, C., Simoneau, P., Keckhut, P., and Hauchecorne, A.: Comparisons of spectrally resolved nightglow emission locally simulated with space and ground level observations, J. Space Weather Spac., 10, 21, https://doi.org/10.1051/swsc/2020017, 2020.

Berger, U. and von Zahn, U.: The two-level structure of the mesopause: A model study, J. Geophys. Res.-Atmos., 104, 22083–22093, https://doi.org/10.1029/1999jd900389, 1999.

Bittner, M., Offermann, D., and Graef, H. H.: Mesopause temperature variability above a midlatitude station in Europe, J. Geophys. Res.-Atmos., 105, 2045–2058, https://doi.org/10.1029/1999jd900307, 2000.

Bittner, M., Höppner, K., Pilger, C., and Schmidt, C.: Mesopause temperature perturbations caused by infrasonic waves as a potential indicator for the detection of tsunamis and other geo-hazards, Nat. Hazards Earth Syst. Sci., 10, 1431–1442, https://doi.org/10.5194/nhess-10-1431-2010, 2010.

Bovensmann, H., Buchwitz, M., Frerick, J., Hoogeveen, R., Kleipool, Q., Lichtenberg, G., Noel, S., Richter, A., Rozanov, A., Rozanov, V., Skupin, J., von Savigny, C., Wuttke, M., and Burrows, J.: SCIAMACHY on ENVISAT: in-flight optical performance and first results, Proc. SPIE 5235, Remote Sensing of Clouds and the Atmosphere VIII, (16 February 2004), 5235, https://doi.org/10.1117/12.514228, 2004.

Brasseur, G. P. and Solomon, S.: Aeronomy of the middle atmosphere, 2nd Edn., D. Reidel Publishing Company, ISBN 9027723443, 1986.

Chadney, J. M., Whiter, D. K., and Lanchester, B. S.: Effect of water vapour absorption on hydroxyl temperatures measured from Svalbard, Ann. Geophys., 35, 481–491, https://doi.org/10.5194/angeo-35-481-2017, 2017.

Chen, Q., Kaufmann, M., Zhu, Y., Liu, J., Koppmann, R., and Riese, M.: Global nighttime atomic oxygen abundances from GOMOS hydroxyl airglow measurements in the mesopause region, Atmos. Chem. Phys., 19, 13891–13910, https://doi.org/10.5194/acp-19-13891-2019, 2019.

Cosby, P. and Slanger, T.: OH spectroscopy and chemistry investigated with astronomical sky spectra, Can. J. Phys., 85, 77–99, 2007.

Danilov, A. D.: Mechanism of red oxygen line excitation in night airglow, Planet. Space Sci., 9, 499–502, https://doi.org/10.1016/0032-0633(62)90053-3, 1962.

Espy, P. and Hammond, M.: Atmospheric transmission coefficients for hydroxyl rotational lines used in rotational temperature determinations, J. Quant. Spectrosc. Ra., 54, 879–889, 1995.

Espy, P. and Stegman, J.: Trends and variability of mesospheric temperature at high-latitudes, Phys. Chem. Earth, Parts A/B/C, 27, 543–553, 2002.

Franzen, C., Espy, P. J., Hibbins, R. E., and Djupvik, A. A.: Observation of Quasiperiodic Structures in the Hydroxyl Airglow on Scales Below 100 m, J. Geophys. Res.-Atmos., 123, 10935–10942, 2018.

French, W., Burns, G., Finlayson, K., Greet, P., Lowe, R., and Williams, P.: Hydroxyl (6/2) airglow emission intensity ratios for rotational temperature determination, Ann. Geophys., 18, 1293–1303, 2000.

French, W. J. R., Mulligan, F. J., and Klekociuk, A. R.: Analysis of 24 years of mesopause region OH rotational temperature observations at Davis, Antarctica – Part 1: long-term trends, Atmos. Chem. Phys., 20, 6379–6394, https://doi.org/10.5194/acp-20-6379-2020, 2020.

Gao, H., Xu, J., Ward, W., Smith, A. K., and Chen, G. M.: Double-layer structure of OH dayglow in the mesosphere, J. Geophys. Res.-Space, 120, 5778–5787, https://doi.org/10.1002/2015ja021208, 2015.

Gault, W., Brown, S., Moise, A., Liang, D., Sellar, G., Shepherd, G., and Wimperis, J.: ERWIN: an E-region wind interferometer, Appl. Opt., 35, 2913–2922, 1996.

Good, R. E.: Determination of atomic oxygen density from rocket borne measurement of hydroxyl airglow, Planet. Space Sci., 24, 389–395, https://doi.org/10.1016/0032-0633(76)90052-0, 1976.

Greet, P. A., French, W. J. R., Burns, G. B., Williams, P. F. B., Lowe, R. P., and Finlayson, K.: OH(6-2) spectra and rotational temperature measurements at Davis, Antarctica, Ann. Geophys.-Atm. Hydr., 16, 77–89, https://doi.org/10.1007/s00585-997-0077-3, 1998.

Grygalashvyly, M.: Several notes on the OH* layer, Ann. Geophys., 33, 923–930, 2015.

Grygalashvyly, M., Sonnemann, G., Lübken, F. J., Hartogh, P., and Berger, U.: Hydroxyl layer: Mean state and trends at midlatitudes, J. Geophys. Res.-Atmos., 119, 12391–12419, 2014.

Hannawald, P., Schmidt, C., Wüst, S., and Bittner, M.: A fast SWIR imager for observations of transient features in OH airglow, Atmos. Meas. Tech., 9, 1461–1472, https://doi.org/10.5194/amt-9-1461-2016, 2016.

Hannawald, P., Schmidt, C., Sedlak, R., Wüst, S., and Bittner, M.: Seasonal and intra-diurnal variability of small-scale gravity waves in OH airglow at two Alpine stations, Atmos. Meas. Tech., 12, 457–469, https://doi.org/10.5194/amt-12-457-2019, 2019.

Harlander, J. M., Roesler, F. L., Cardon, J. G., Englert, C. R., and Conway, R. R.: Shimmer: a spatial heterodyne spectrometer for remote sensing of Earth'middle atmosphere, Appl. Opt., 41, 1343–1352, 2002.

Harrison, A. and Kendall, D.: Airglow hydroxyl intensity measurements $0 \cdot 6 - 2 \cdot 3 \mu$, Planet. Space Sci., 21, 1731–1741, 1973.

Heaps, H. and Herzberg, G.: Intensity distribution in the rotation-vibration spectrum of the OH molecule, Z. Phys., 133, 48–64, 1952.

Hecht, J., Walterscheid, R., Sivjee, G., Christensen, A., and Pranke, J.: Observations of wave-driven fluctuations of OH nightglow emission from Sondre Stromfjord, Greenland, J. Geophys. Res.-Space, 92, 6091–6099, 1987.

Hecht, J. H.: Instability layers and airglow imaging, Rev. Geophys., 42, RG1001, https://doi.org/10.1029/2003RG000131, 2004.

Hecht, J. H., Fritts, D. C., Gelinas, L. J., Rudy, R. J., Walterscheid, R. L., and Liu, A. Z.: Kelvin-Helmholtz billow interactions and instabilities in the mesosphere over the Andes Lidar Observatory:

1. Observations, J. Geophys. Res.-Atmos., 126, e2020JD033414 https://doi.org/10.1029/2020JD033414, 2021.

Herzberg, G.: The atmospheres of the planets, J. Roy. Astro. Soc. Can., 45, 100, https://articles.adsabs.harvard.edu/pdf/1951JRASC..45..100H (last access: 12 January 2023), 1951.

Inchin, P. A., Snively, J. B., Williamson, A., Melgar, D., Guerrero, J. A., and Zettergren, M. D.: Mesopause airglow disturbances driven by nonlinear infrasonic acoustic waves generated by large earthquakes, J. Geophys. Res.-Space, 125, e2019JA027628, https://doi.org/10.1029/2019JA027628, 2020.

Jacobi, C., Arras, C., Kürschner, D., Singer, W., Hoffmann, P., and Keuer, D.: Comparison of mesopause region meteor radar winds, medium frequency radar winds and low frequency drifts over Germany, Adv. Space Res., 43, 247–252, https://doi.org/10.1016/j.asr.2008.05.009, 2009.

Khomich, V. Y., Semenov, A. I., and Shefov, N. N.: Airglow as an indicator of upper atmospheric structure and dynamics, Springer Science & Business Media, ISBN 9783540758327, 2008.

Krassovsky, V., Shefov, N., and Yarin, V.: Atlas of the airglow spectrum 3000–12400 Å, Planet. Space Sci., 9, 883–915, 1962.

Krassovsky, V. I.: On the mechanism of the night sky luminescence, Doklady Akademii Nauk SSSR, 395–398, 1951.

Krassovsky, V. I.: Chemistry of the upper atmosphere, Space Research Conference, Space Research III, edited by: Priester, W., Proceedings of the Third International Space Science Symposium, Washington, D.C., USA, 2–8 May, 96–116, 1963.

Krassovsky, V. I.: Infrasonic variations of OH emission in the upper atmosphere, Ann. Geophys., 28, 739–746, 1972.

Kristl, J., Esplin, M., Hudson, T., Taylor, M., and Siefring, C. L.: Preliminary data on variations of OH airglow during the Leonid 1999 meteor storm, Earth, Moon and Planets, 82, 525–534, 2000.

Kristoffersen, S. K., Ward, W. E., Brown, S., and Drummond, J. R.: Calibration and validation of the advanced E-Region Wind Interferometer, Atmos. Meas. Tech., 6, 1761–1776, https://doi.org/10.5194/amt-6-1761-2013, 2013.

Kyrölä, E., Tamminen, J., Leppelmeier, G., Sofieva, V., Hassinen, S., Bertaux, J., Hauchecorne, A., Dalaudier, F., Cot, C., Korablev, O., Fanton d'Andon, O., Snoejj, P., Koopmann, R., Saavedra, L., Fraisse, R., Fussen, D., and Vanhellemont, F.: GOMOS on Envisat: An overview, Adv. Space Res., 33, 1020–1028, 2004.

Lai, C., Xu, J. Y., Yue, J., Yuan, W., Liu, X., Li, W., and Li, Q. Z.: Automatic extraction of gravity waves from all-sky airglow image based on machine learning, Remote Sens., 11, 1516, https://doi.org/10.3390/rs11131516, 2019.

Langille, J. A., Ward, W. E., Scott, A., and Arsenault, D. L.: Measurement of two-dimensional Doppler wind fields using a field widened Michelson interferometer, Appl. Opt., 52, 1617–1628, 2013.

Le Du, T., Simoneau, P., Keckhut, P., Hauchecorne, A., and Le Pichon, A.: Investigation of infrasound signatures from microbaroms using OH airglow and ground-based microbarometers. Adv. Space Res., 65, 902–908, https://doi.org/10.1016/j.asr.2019.11.026, 2020.

Li, T., She, C. Y., Williams, B. P., Yuan, T., Collins, R. L., Kieffaber, L. M., and Peterson, A. W.: Concurrent OH imager and sodium temperature/wind lidar observation of localized ripples over northern Colorado, J. Geophys. Res.-Atmos., 110, D13110, https://doi.org/10.1029/2004JD004885, 2005.

Li, J., Li, T., Dou, X., Fang, X., Cao, B., She, C.-Y., Nakamura, T., Manson, A., Meek, C., and Thorsen, D.: Characteristics of ripple structures revealed in OH airglow images, J. Geophys. Res.-Space, 122, 3748–3759, https://doi.org/10.1002/2016JA023538, 2017.

Liu, G. and Shepherd, G. G.: An empirical model for the altitude of the OH nightglow emission, Geophys. Res. Lett., 33, L09805, https://doi.org/10.1029/2005gl025297, 2006.

Llewellyn, E., Degenstein, D., Lloyd, N., Gattinger, R., Petelina, S., McDade, I., Haley, C., Solheim, B., von Savigny, C., and Sioris, C.: First Results from the OSIRIS Instrument on-board Odin, Sodankylä Geophysical Observatory Publications, 92, 41–47, 2003.

Llewellyn, E. J., Lloyd, N. D., Degenstein, D. A., Gattinger, R. L., Petelina, S. V., Bourassa, A. E., Wiensz, J. T., Ivanov, E. V., McDade, I. C., Solheim, B. H., McConnell, J. C., Haley, C. S., Savigny, C. v., Sioris, C. E., McLinden, C. A., Griffioen, E., Kaminski, J., Evans, W. F., Puckrin, E., Strong, K., Wehrle, V., Hum, R. H., Kendall, D. J., Matsushita, J., Murtagh, D. P., Brohede, S., Stegman, J., Witt, G., Barnes, G., Payne, W. F., Piché, L., Smith, K., Warshaw, G., Deslauniers, D.-L., Marchand, P., Richardson, E. H., King, R. A., Wevers, I., McCreath, W., Kyrölä, E., Oikarinen, L., Leppelmeier, G. W., Auvinen, H., Mégie, G., Hauchecorne, A., Lefèvre, F., Nöe, J. d. L., Ricaud, P., Frisk, U., Sjoberg, F., Schéele, F. v., and Nordh, L.: The OSIRIS instrument on the Odin spacecraft, Can. J. Phys., 82, 411–422, https://doi.org/10.1139/p04-005, 2004.

López-González, M. J., García-Comas, M., Rodríguez, E., López-Puertas, M., Shepherd, M. G., Shepherd, G. G., Sargoytchev, S., Aushev, V. M., Smith, S. M., Mlynczak, M. G., Russell, J. M., Brown, S., Cho, Y. M., and Wiens, R. H.: Ground-based mesospheric temperatures at mid-latitude derived from O$_2$ and OH airglow SATI data: Comparison with SABER measurements, J. Atmos. Sol.-Terr. Phy., 69, 2379–2390, https://doi.org/10.1016/j.jastp.2007.07.004, 2007.

López-González, M. J., García-Comas, M., Rodríguez, E., López-Puertas, M., Olivares, I., Jeronimo-Zafra, J. M., Robles-Munoz, N. F., Perez-Silvente, T., Shepherd, M. G., Shepherd, G. G., and Sargoytchev, S.: Gravity wave activity in the middle atmosphere from SATI airglow observations at northern mid-latitude: Seasonal variation and comparison with tidal and planetary wave-like activity, J. Atmos. So.-Terr. Phy., 206, 105329, https://doi.org/10.1016/j.jastp.2020.105329, 2020.

Lowe, R. P., LeBlanc, L. M., and Gilbert, K. L.: WINDII/UARS observation of twilight behaviour of the hydroxyl airglow, at mid-latitude equinox, J. Atmos. Terr. Phys., 58, 1863–1869, https://doi.org/10.1016/0021-9169(95)00178-6, 1996.

Lübken, F. J. and von Zahn, U.: Thermal structure of the mesopause region at polar latitudes, J. Geophys. Res.-Atmos., 96, 20841–20857, https://doi.org/10.1029/91jd02018, 1991.

Marsh, D. R., Smith, A. K., Mlynczak, M. G., and Russell III, J. M.: SABER observations of the OH Meinel airglow variability near the mesopause, J. Geophys. Res.-Space, 111, A10S05, https://doi.org/10.1029/2005JA011451, 2006.

Marshall, R. A., Smith, S., Baumgardner, J., and Chakrabarti, S.: Continuous ground-based multiwavelength airglow measurements, J. Geophys. Res.-Space, 116, A11304, https://doi.org/10.1029/2011JA016901, 2011.

Meinel, A. B.: OH emission bands in the spectrum of the night sky II, Astrophys. J., 112, 120, https://adsabs.harvard.edu/pdf/1950ApJ...112..120M (last access: 12 January 2023), 1950a.

Meinel, A. B.: OH emission bands in the spectrum of the night sky I, Astrophys. J., 111, 555, https://adsabs.harvard.edu/pdf/1950ApJ...111..555M (last access: 12 January 2023), 1950b.

Miller, S. D., Mills, S. P., Elvidge, C. D., Lindsey, D. T., Lee, T. F., and Hawkins, J. D.: Suomi satellite brings to light a unique frontier of nighttime environmental sensing capabilities, P. Natl. Acad. Sci. USA, 109, 15706–15711, 2012.

Miller, S. D., Straka, W. C., Yue, J., Smith, S. M., Alexander, M. J., Hoffmann, L., Setvák, M., and Partain, P. T.: Upper atmospheric gravity wave details revealed in nightglow satellite imagery, P. Natl. Acad. Sci. USA, 112, E6728–E6735, 2015.

Misawa, K. and Takeuchi, I.: Ground observation of the O_2 (0-1) atmospheric band at 8645 Å and the [OI] 5577-Å line, J. Geophys. Res., 82, 2410–2412, 1977.

Misawa, K. and Takeuchi, I.: Correlations among O2 (0–1) atmospheric band, OH (8–3) band and [OI] 5577 Å line and among P1 (2), P1 (3) and P1 (4) lines of OH (8–3) band, J. Atmos. Terr. Phys., 40, 421–428, 1978.

Moreels, G., Megie, G., Jones, A. V., and Gattinger, R. L.: Oxygen-hydrogen atmospheric model and its application to OH-emission problem, J. Atmos. Terr. Phys., 39, 551–570, https://doi.org/10.1016/0021-9169(77)90065-4, 1977.

Mulligan, F., Horgan, D., Galligan, J., and Griffin, E.: Mesopause temperatures and integrated band brightnesses calculated from airglow OH emissions recorded at Maynooth (53.2° N, 6.4° W) during 1993, J. Atmos. Terr. Phys., 57, 1623–1637, 1995.

Mulligan, F., Dyrland, M., Sigernes, F., and Deehr, C.: Inferring hydroxyl layer peak heights from ground-based measurements of OH(6-2) band integrated emission rate at Longyearbyen (78° N, 16° E), Ann. Geophys., 27, 4197–4205, 2009.

Nappo, C. J.: An introduction to atmospheric gravity waves, Academic Press, ISBN 9780123852236, 2013.

Nee, J. B., Tsai, S. D., Peng, T. H., Hsu, R. R., Chen, A. B. C., Zhang, S. P., Huang, T. Y., Rajesh, P. K., Liu, J. Y., Frey, H. U., and Mende, S. B.: OH airglow and equatorial variations observed by ISUAL Instrument on board the FORMOSAT 2 satellite, Terr. Atmos. Ocean. Sci., 21, 985–995, https://doi.org/10.3319/Tao.2010.03.12.01(Aa), 2010.

Nicolet, M.: Aeronomic chemistry of ozone, Planet. Space Sci., 37, 1621–1652, https://doi.org/10.1016/0032-0633(89)90150-5, 1989.

Nicovich, J. M. and Wine, P. H.: Temperature-dependence of the O+ HO_2 Rate Coefficient, J. Phys. Chem., 91, 5118–5123, https://doi.org/10.1021/j100303a049, 1987.

Noll, S., Kausch, W., Kimeswenger, S., Barden, M., Jones, A., Modigliani, A., Szyszka, C., and Taylor, J.: Skycorr: A general tool for spectroscopic sky subtraction, Journal of Astronomy and Astrophysics, 567, A25, https://doi.org/10.1051/0004-6361/201423908, 2014.

Noll, S., Kausch, W., Kimeswenger, S., Unterguggenberger, S., and Jones, A. M.: Comparison of VLT/X-shooter OH and O_2 rotational temperatures with consideration of TIMED/SABER emission and temperature profiles, Atmos. Chem. Phys., 16, 5021–5042, https://doi.org/10.5194/acp-16-5021-2016, 2016.

Noll, S., Kimeswenger, S., Proxauf, B., Unterguggenberger, S., Kausch, W., and Jones, A. M.: 15 years of VLT/UVES OH intensities and temperatures in comparison with TIMED/SABER data, J. Atmos. Sol.-Terr. Phy., 163, 54–69, https://doi.org/10.1016/j.jastp.2017.05.012, 2017.

Noll, S., Winkler, H., Goussev, O., and Proxauf, B.: OH level populations and accuracies of Einstein-A coefficients from hundreds of measured lines, Atmos. Chem. Phys., 20, 5269–5292, https://doi.org/10.5194/acp-20-5269-2020, 2020.

Noxon, J.: The latitude dependence of OH rotational temperature in the night airglow, J. Geophys. Res., 69, 4087–4092, 1964.

Offermann, D., Gusev, O., Donner, M., Forbes, J. M., Hagan, M., Mlynczak, M. G., Oberheide, J., Preusse, P., Schmidt, H., and Russell, J. M.: Relative intensities of middle atmosphere waves, J. Geophys. Res.-Atmos., 114, D06110, https://doi.org/10.1029/2008jd010662, 2009.

Oliva, E., Origlia, L., Scuderi, S., Benatti, S., Carleo, I., Lapenna, E., Mucciarelli, A., Baffa, C., Biliotti, V., and Carbonaro, L.: Lines and continuum sky emission in the near infrared: observational constraints from deep high spectral resolution spectra with GIANO-TNG, Astron. Astrophys., 581, A47, https://doi.org/10.1051/0004-6361/201526291, 2015.

Pallamraju, D., Baumgardner, J., and Chakrabarti, S.: HIRISE: a ground-based high-resolution imaging spectrograph using echelle grating for measuring daytime airglow/auroral emissions, J. Atmos. Sol.-Terr. Phy., 64, 1581–1587, https://doi.org/10.1016/S1364-6826(02)00095-0, 2002.

Pautet, P. D., Taylor, M. J., Pendleton, W. R., Zhao, Y., Yuan, T., Esplin, R., and McLain, D.: Advanced mesospheric temperature mapper for high-latitude airglow studies, Appl. Opt., 53, 5934–5943, https://doi.org/10.1364/AO.53.005934, 2014.

Pautet, P. D., Taylor, M. J., Eckermann, S., and Criddle, N.: Regional distribution of mesospheric small-scale gravity waves during DEEPWAVE, J. Geophys. Res.-Atmos., 124, 7069–7081, 2019.

Pendleton Jr, W., Espy, P., and Hammond, M.: Evidence for non-local-thermodynamic-equilibrium rotation in the OH nightglow, J. Geophys. Res.-Space, 98, 11567–11579, 1993.

Pilger, C., Schmidt, C., and Bittner, M.: Statistical analysis of infrasound signatures in airglow observations: Indications for acoustic resonance, J. Atmos. Sol.-Terr. Phy., 93, 70–79, https://doi.org/10.1016/j.jastp.2012.11.011, 2013a.

Pilger, C., Schmidt, C., Streicher, F., Wüst, S., and Bittner, M.: Airglow observations of orographic, volcanic and meteorological infrasound signatures, J. Atmos. Sol.-Terr. Phys., 104, 55–66, https://doi.org/10.1016/j.jastp.2013.08.008, 2013b.

Rajesh, P., Liu, J., Chiang, C., Chen, A., Chen, W., Su, H.-T., Hsu, R.-R., Lin, C., Hsu, M. L., and Yee, J.: First results of the limb imaging of 630.0 nm airglow using FORMOSAT-2/Imager of Sprites and Upper Atmospheric Lightnings, J. Geophys. Res.-Space, 114, A10302, https://doi.org/10.1029/2009JA014087, 2009.

Rauthe, M., Gerding, M., Höffner, J., and Lübken, F. J.: Lidar temperature measurements of gravity waves over Kühlungsborn (54° N) from 1 to 105 km: A winter-summer comparison, J. Geophys. Res., 111, D24108, https://doi.org/10.1029/2006jd007354, 2006.

Reisin, E. R. and Scheer, J.: Vertical propagation of gravity waves determined from zenith observations of airglow, Adv. Space Res., 27, 1743–1748, 2001.

Reisin, E. R., Scheer, J., Dyrland, M. E., Sigernes, F., Deehr, C. S., Schmidt, C., Höppner, K., Bittner, M., Ammosov, P. P., Gavrilyeva, G. A., Stegman, J., Perminov, V. I., Semenov, A. I., Knieling, P., Koppmann, R., Shiokawa, K., Lowe, R. P., López-González, M. J., Rodríguez, E., Zhao, Y., Taylor, M. J., Buriti, R. A., Espy, P. J., French, W. J. R., Eichmann, K. U., Burrows, J. P., and von Savigny, C.: Traveling planetary wave activity from mesopause region airglow temperatures determined by the Network for the Detection of Mesospheric Change (NDMC). J. Atmos. Sol.-Terr. Phys. 119, 71–82, https://doi.org/10.1016/j.jastp.2014.07.002, 2014.

Richter, H., Buchbender, C., Güsten, R., Higgins, R., Klein, B., Stutzki, J., Wiesemeyer, H., and Hübers, H.-W. J. C. E.: Direct measurements of atomic oxygen in the mesosphere and lower thermosphere using terahertz heterodyne spectroscopy, Communications Earth and Environment, 2, 1–9, https://doi.org/10.1038/s43247-020-00084-5, 2021.

Roach, F. and Gordon, J. L.: The Night Airglow Or Nightglow, in: The Light of the Night Sky, Springer, 47–81, ISBN 9027702934, 1973.

Rodrigo, R., Lopez-Gonzalez, M., and Lopez-Moreno, J.: Variability of the neutral mesospheric and lower thermospheric composition in the diurnal cycle, Planet. Space Sci., 39, 803–820, 1991.

Rourke, S., Mulligan, F. J., French, W. J. R., and Murphy, D. J.: A climatological study of short-period gravity waves and ripples at Davis Station, Antarctica (68° S, 78° E), during the (austral winter February–October) period 1999–2013, J. Geophys. Res.-Atmos., 122, 11388–11404, https://doi.org/10.1002/2017JD026998, 2017.

Rousselot, P., Lidman, C., Cuby, J. G., Moreels, G., and Monnet, G.: Night-sky spectral atlas of OH emission lines in the near-infrared, Astron. Astrophys., 354, 1134–1150, 2000.

Russell III, J. M., Mlynczak, M. G., Gordley, L. L., Tansock Jr, J. J., and Esplin, R. W.: Overview of the SABER experiment and preliminary calibration results, P. Soc. Photo.-Opt. Ins., 3756, 277–288, 1999.

Sargoytchev, S. I., Brown, S., Solheim, B. H., Cho, Y.-M., Shepherd, G. G., and López-González, M. J.: Spectral airglow temperature imager (SATI): a ground-based instrument for the monitoring of mesosphere temperature, Appl. Opt., 43, 5712–5721, 2004.

Scheer, J.: Programmable tilting filter spectrometer for studying gravity waves in the upper atmosphere, Appl. Opt., 26, 3077–3082, 1987.

Schmidt, C., Höppner, K., and Bittner, M.: A ground-based spectrometer equipped with an InGaAs array for routine observations of OH(3-1) rotational temperatures in the mesopause region, J. Atmos. Sol.-Terr. Phy., 102, 125–139, https://doi.org/10.1016/j.jastp.2013.05.001, 2013.

Schmidt, C., Dunker, T., Lichtenstern, S., Scheer, J., Wüst, S., Hoppe, U. P., and Bittner, M.: Derivation of vertical wavelengths of gravity waves in the MLT-region from multispectral airglow observations, J. Atmos. Sol.-Terr. Phy., 173, 119–127, https://doi.org/10.1016/j.jastp.2018.03.002, 2018.

Sedlak, R., Hannawald, P., Schmidt, C., Wüst, S., and Bittner, M.: High-resolution observations of small-scale gravity waves and turbulence features in the OH airglow layer, Atmos. Meas. Tech., 9, 5955–5963, https://doi.org/10.5194/amt-9-5955-2016, 2016.

Sedlak, R., Zuhr, A., Schmidt, C., Wüst, S., Bittner, M., Didebulidze, G. G., and Price, C.: Intra-annual variations of spectrally resolved gravity wave activity in the upper mesosphere/lower thermosphere (UMLT) region, Atmos. Meas. Tech., 13, 5117–5128, https://doi.org/10.5194/amt-13-5117-2020, 2020.

Sedlak, R., Hannawald, P., Schmidt, C., Wüst, S., Bittner, M., and Stanič, S.: Gravity wave instability structures and turbulence from more than 1.5 years of OH* airglow imager observations in Slovenia, Atmos. Meas. Tech., 14, 6821–6833, https://doi.org/10.5194/amt-14-6821-2021, 2021.

She, C. Y., Yu, J. R., and Chen, H.: Observed thermal structure of a midlatitude mesopause, Geophys. Res. Lett., 20, 567–570, https://doi.org/10.1029/93gl00808, 1993.

She, C. Y., Chen, S., Hu, Z., Sherman, J., Vance, J. D., Vasoli, V., White, M. A., Yu, J., and Krueger, D. A.: Eight-year climatology of nocturnal temperature and sodium density in the mesopause region (80 to 105 km) over Fort Collins, CO (41° N, 105° W), Geophys. Res. Lett., 27, 3289–3292, https://doi.org/10.1029/2000GL003825, 2000.

Sheese, P., Llewellyn, E., Gattinger, R., Bourassa, A., Degenstein, D., Lloyd, N., and McDade, I.: Mesopause temperatures during the polar mesospheric cloud season, Geophys. Res. Lett., 38, L11803, https://doi.org/10.1029/2011GL047437, 2011.

Sheese, P. E., Llewellyn, E. J., Gattinger, R. L., and Strong, K.: OH Meinel band nightglow profiles from OSIRIS observations, J. Geophys. Res.-Atmos., 119, 11417–11428, https://doi.org/10.1002/2014jd021617, 2014.

Shemansky, D. and Jones, A. V.: New measurements of the night airglow spectrum in the 1.5 μ region, J. Atmos. Terr. Phys., 22, 166–175, 1961.

Shepherd, G. G., Thuillier, G., Gault, W. A., Solheim, B. H., Hersom, C., Alunni, J. M., Brun, J. F., Brune, S., Charlot, P., Cogger, L. L., Desaulniers, D. L., Evans, W. F. J., Gattinger, R. L., Girod, F., Harvie, D., Hum, R. H., Kendall, D. J. W., Llewellyn, E. J., Lowe, R. P., Ohrt, J., Pasternak, F., Peillet, O., Powell, I., Rochon, Y., Ward, W. E., Wiens, R. H., and Wimperis, J.: WINDII, the Wind Imaging Interferometer on the Upper-Atmosphere Research Satellite, J. Geophys. Res.-Atmos., 98, 10725–10750, https://doi.org/10.1029/93jd00227, 1993.

Shepherd, G. G., Thuillier, G., Cho, Y. M., Duboin, M. L., Evans, W. F., Gault, W., Hersom, C., Kendall, D., Lathuillere, C., Lowe, R., McDade, I. C., Rochon, Y., Shepherd, M., Solheim, B. H., Wang, D., and Ward, W.: The wind imaging interferometer (WINDII) on the upper atmosphere research satellite: a 20 year perspective, Rev. Geophys., 50, RG2007, https://doi.org/10.1029/2012RG000390, 2012.

Shepherd, M. G., Meek, C. E., Hocking, W. K., Hall, C. M., Partamies, N., Sigernes, F., Manson, A. H., and Ward, W. E.: Multi-instrument study of the mesosphere-lower thermosphere dynamics at 80° N during the major SSW in January 2019, 2020.

Shiokawa, K., Kadota, T., Ejiri, M. K., Otsuka, Y., Katoh, Y., Satoh, M., and Ogawa, T.: Three-channel imaging Fabry–Perot interferometer for measurement of mid-latitude airglow, Appl. Opt., 40, 4286–4296, 2001.

Siefring, C. L., Morrill, J. S., Sentman, D. D., and Heavner, M. J.: Simultaneous near-infrared and visible observations of sprites and acoustic-gravity waves during the EXL98 campaign, J. Geophys. Res.-Space, 115, A00E57, https://doi.org/10.1029/2009JA014862, 2010.

Sigernes, F., Shumilov, N., Deehr, C., Nielsen, K., Svenøe, T., and Havnes, O.: Hydroxyl rotational temperature record from the auroral station in Adventdalen, Svalbard (78° N, 15° E), J. Geophys. Res.-Space, 108, 1342, https://doi.org/10.1029/2001JA009023, 2003.

Silber, I., Price, C., Schmidt, C., Wüst, S., Bittner, M., and Pecora, E.: First ground-based observations of mesopause temperatures above the Eastern-Mediterranean Part I: Multi-day oscillations and tides, J. Atmos. Sol.-Terr. Phy., 155, 95–103, 2017.

Sivjee, G. and Hamwey, R.: Temperature and chemistry of the polar mesopause OH, J. Geophys. Res.-Space, 92, 4663–4672, 1987.

Sivjee, G. G.: Airglow hydroxyl emissions, Planet. Space Sci., 40, 235–242, https://doi.org/10.1016/0032-0633(92)90061-R, 1992.

Smette, A., Sana, H., Noll, S., Horst, H., Kausch, W., Kimeswenger, S., Barden, M., Szyszka, C., Jones, A., and Gallenne, A.: Molecfit: A general tool for telluric absorption correction – I. Method and application to ESO instruments, Astron. Astrophys., 576, A77, https://doi.org/10.1051/0004-6361/201423932, 2015.

Smith, A. K., Marsh, D. R., Mlynczak, M. G., and Mast, J. C.: Temporal variations of atomic oxygen in the upper mesosphere from SABER, J. Geophys. Res.-Atmos., 115, D18309, https://doi.org/10.1029/2009JD013434, 2010.

Snively, J. B., Pasko, V. P., and Taylor, M. J.: OH and OI airglow layer modulation by ducted short-period gravity waves: Effects of trapping altitude, J. Geophys. Res.-Space, 115, A11311, https://doi.org/10.1029/2009ja015236, 2010.

Sridharan, R., Modl, N. K., Raju, D. P., Narayanan, R., Pant, T. K., Taori, A., and Chakrabarty, D.: A multiwavelength daytime photometer - a new tool for the investigation of atmospheric processes, Meas. Sci. Technol., 9, 585–591, https://doi.org/10.1088/0957-0233/9/4/005, 1998.

Stehr, J., Knieling, P., Olschewski, F., Mantel, K., Kaufmann, M., and Koppmann, R.: GRIPS-HI, a novel spectral imager for ground based measurements of mesopause temperatures, tm – Technisches Messen, 88, 655–660, https://doi.org/10.1515/teme-2021-0043, 2021.

Suzuki, H., Shiokawa, K., Tsutsumi, M., Nakamura, T., and Taguchi, M.: Atmospheric gravity waves identified by ground-based observations of the intensity and rotational temperature of OH airglow, Polar Science, 2, 1–8, 2008.

Suzuki, S., Shiokawa, K., Otsuka, Y., Ogawa, T., Kubota, M., Tsutsumi, M., Nakamura, T., and Fritts, D. C.: Gravity wave momentum flux in the upper mesosphere derived from OH airglow imaging measurements, Earth Planets Space, 59, 421–428, https://doi.org/10.1186/Bf03352703, 2007.

Swenson, G. and Espy, P. J.: Observations of 2-dimensional airglow structure and Na density from the ALOHA, 9 October 1993 "storm flight", Geophys. Res. Lett., 22, 2845–2848, 1995.

Swenson, G. R. and Gardner, C. S.: Analytical models for the responses of the mesospheric OH* and Na layers to atmospheric gravity waves, J. Geophys. Res.-Atmos., 103, 6271–6294, 1998.

Swenson, G. R. and Liu, A. Z.: A model for calculating acoustic gravity wave energy and momentum flux in the mesosphere from OH airglow, Geophys. Res. Lett., 25, 477–480, https://doi.org/10.1029/98gl00132, 1998.

Takahashi, H., Batista, P. P., Sahai, Y., and Clemesha, B. R.: Atmospheric wave propagations in the mesopause region observed by the OH (8, 3) band, NaD, O_2A (8645Å) band and OI 5577 Å nightglow emissions, Planet. Space Sci., 33, 381–384, https://doi.org/10.1016/0032-0633(85)90081-9, 1985.

Tang, J., Liu, A., and Swenson, G.: High frequency gravity -waves observed in OH airglow at Starfire Optical Range, NM; seasonal variations in momentum flux, GRL, 29, 27-1–27-4, 2002.

Taylor, M. J.: A review of advances in imaging techniques for measuring short period gravity waves in the mesosphere and lower thermosphere, Middle and Upper Atmospheres: Small Scale Structures and Remote Sens., 19, 667–676, https://doi.org/10.1016/S0273-1177(97)00161-0, 1997.

Taylor, M. J., Bishop, M. B., and Taylor, V.: All-sky measurements of short period gravity waves imaged in the OI(557.7 nm), Na(589.2 nm) and near infrared OH and $O_2(0,1)$ nightglow emissions during the ALOHA-93 campaign, Geophys. Res. Lett., 22, 2833–2836, https://doi.org/10.1029/95GL02946, 1995.

Thorne, A. P.: Emission and absorption of line radiation, in: Spectrophysics, Springer, 286–317, https://doi.org/10.1007/978-94-009-1193-2_11, 1988.

Vadas, S. L., Fritts, D. C., and Alexander, M. J.: Mechanism for the generation of secondary waves in wave breaking regions, J. Atmos. Sciences, 60, 194–214, https://doi.org/10.1175/1520-0469(2003)060<0194:MFTGOS>2.0.CO;2, 2003.

Van Zandt, T. E.: A model for gravity wave spectra observed by Doppler sounding systems, Radio Sci., 20, 1323–1330, 1985.

Vargas, F., Swenson, G., and Liu, A.: Evidence of high frequency gravity wave forcing on the meridional residual circulation at the mesopause region, Adv. Space Res., 56, 1844–1853, https://doi.org/10.1016/j.asr.2015.07.040, 2015.

von Savigny, C.: Variability of OH(3−1) emission altitude from 2003 to 2011: Long-term stability and universality of the emission rate–altitude relationship, J. Atmos. Sol.-Terr. Phy., 127, 120–128, https://doi.org/10.1016/j.jastp.2015.02.001, 2015.

von Savigny, C. and Lednyts' kyy, O.: On the relationship between atomic oxygen and vertical shifts between OH Meinel bands originating from different vibrational levels, Geophys. Res. Lett., 40, 5821–5825, 2013.

von Savigny, C., Eichmann, K. U., Llewellyn, E., Bovensmann, H., Burrows, J., Bittner, M., Höppner, K., Offermann, D., Taylor, M. J., and Zhao, Y.: First near-global retrievals of OH rotational temperatures from satellite-based Meinel band emission measurements, Geophys. Res. Lett., 31, L15111, https://doi.org/10.1029/2004GL020410, 2004.

von Savigny, C., McDade, I. C., Eichmann, K.-U., and Burrows, J. P.: On the dependence of the OH* Meinel emission altitude on vibrational level: SCIAMACHY observations and model simulations, Atmos. Chem. Phys., 12, 8813–8828, https://doi.org/10.5194/acp-12-8813-2012, 2012.

von Zahn, U., Fricke, K., Gerndt, R., and Blix, T.: Mesospheric temperatures and the OH layer height as derived from ground-based lidar and OH* spectrometry, J. Atmos. Terr. Phys., 49, 863–869, 1987.

von Zahn, U., Hoffner, J., Eska, V., and Alpers, M.: The mesopause altitude: Only two distinctive levels worldwide?, Geophys. Res. Lett., 23, 3231–3234, 1996.

Wachter, P., Schmidt, C., Wüst, S., and Bittner, M.: Spatial gravity wave characteristics obtained from multiple OH(3−1) airglow temperature time series, J. Atmos. Sol.-Terr. Phy., 135, 192–201, 2015.

Wang, Z., Huang, M., Sun, Y., Tao, T., Qian, L., Zhang, G., Zhao, B., Han, W., Wang, G., and Zhao, Y.: Near-Earth space balloon-based multi-band airglow imager optic design, Appl. Opt., 60, 8057–8068, 2021.

Waters, J. W., Froidevaux, L., Harwood, R. S., Jarnot, R. F., Pickett, H. M., Read, W. G., Siegel, P. H., Cofield, R. E., Filipiak, M. J., Flower, D. A., Holden, J. R., Lau, G. K. K., Livesey, N. J., Manney, G. L., Pumphrey, H. C., Santee, M. L., Wu, D. L., Cuddy, D. T., Lay, R. R., Loo, M. S., Perun, V. S., Schwartz, M. J., Stek, P. C., Thurstans, R. P., Boyles, M. A., Chandra, K. M., Chavez, M. C., Chen, G. S., Chudasama, B. V., Dodge, R., Fuller, R. A., Girard, M. A., Jiang, J. H., Jiang, Y. B., Knosp, B. W., LaBelle, R. C., Lam, J. C., Lee, K. A., Miller, D., Oswald, J. E., Patel, N. C., Pukala, D. M., Quintero, O., Scaff, D. M., Van Snyder, W., Tope, M. C., Wagner, P. A., and Walch, M. J.: The Earth Observing System Microwave Limb Sounder (EOS MLS) on the Aura satellite, IEEE T. Geosci. Remote, 44, 1075–1092, https://doi.org/10.1109/Tgrs.2006.873771, 2006.

Wiens, R., Moise, A., Brown, S., Sargoytchev, S., Peterson, R., Shepherd, G., Lopez-Gonzalez, M., Lopez-Moreno, J., and Rodrigo, R.: SATI: A spectral airglow temperature imager, Adv. Space Res., 19, 677–680, 1997.

Wolff, M. M.: A new attack on height measurement of the nightglow by ground triangulation, J. Geophys. Res., 71, 2743–2748, https://doi.org/10.1029/JZ071i011p02743, 1966.

Wüst, S. and Bittner, M.: Non-linear resonant wave-wave interaction (triad): Case studies based on rocket data and first application to satellite data, J. Atmos. Sol.-Terr. Phy., 68, 959–976, 2006.

Wüst, S., Wendt, V., Schmidt, C., Lichtenstern, S., Bittner, M., Yee, J. H., Mlynczak, M. G., and Russell, J. M.: Derivation of gravity wave potential energy density from NDMC measurements, J. Atmos. Sol.-Terr. Phy., 138, 32–46, https://doi.org/10.1016/j.jastp.2015.12.003, 2016.

Wüst, S., Bittner, M., Yee, J.-H., Mlynczak, M. G., and Russell III, J. M.: Variability of the Brunt–Väisälä frequency at the OH* layer height, Atmos. Meas. Tech., 10, 4895–4903, https://doi.org/10.5194/amt-10-4895-2017, 2017.

Wüst, S., Offenwanger, T., Schmidt, C., Bittner, M., Jacobi, C., Stober, G., Yee, J.-H., Mlynczak, M. G., and Russell III, J. M.: Derivation of gravity wave intrinsic parameters and vertical wavelength using a single scanning OH(3-1) airglow spectrometer, Atmos. Meas. Tech., 11, 2937–2947, https://doi.org/10.5194/amt-11-2937-2018, 2018.

Wüst, S., Schmidt, C., Hannawald, P., Bittner, M., Mlynczak, M. G., and Russell III, J. M.: Observations of OH airglow from ground, aircraft, and satellite: investigation of wave-like structures before a minor stratospheric warming, Atmos. Chem. Phys., 19, 6401–6418, https://doi.org/10.5194/acp-19-6401-2019, 2019.

Wüst, S., Bittner, M., Yee, J.-H., Mlynczak, M. G., and Russell III, J. M.: Variability of the Brunt–Väisälä frequency at the OH*-airglow layer height at low and midlatitudes, Atmos. Meas. Tech., 13, 6067–6093, https://doi.org/10.5194/amt-13-6067-2020, 2020.

Xu, J., Gao, H., Smith, A. K., and Zhu, Y.: Using TIMED/SABER nightglow observations to investigate hydroxyl emission mechanisms in the mesopause region, J. Geophys. Res.-Atmos., 117, D02301, https://doi.org/10.1029/2011JD016342, 2012.

Xu, S., Yue, J., Xue, X., Vadas, S. L., Miller, S. D., Azeem, I., Straka III, W., Hoffmann, L., and Zhang, S.: Dynamical coupling between hurricane matthew and the middle to upper atmosphere via gravity waves, J. Geophys. Res.-Space, 124, 3589–3608, 2019.

Yue, J., Miller, S. D., Hoffmann, L., and Straka III, W. C.: Stratospheric and mesospheric concentric gravity waves over tropical cyclone Mahasen: Joint AIRS and VIIRS satellite observations, J. Atmos. Sol.-Terr. Phys., 119, 83–90, 2014.

Yue, J., Perwitasari, S., Xu, S., Hozumi, Y., Nakamura, T., Sakanoi, T., Saito, A., Miller, S. D., Straka, W., and Rong, P.: Preliminary dual-satellite observations of atmospheric gravity waves in airglow, Atmosphere, 10, 650, https://doi.org/10.3390/atmos10110650, 2019.

Zhou, X., Holton, J. R., Mullendore, G. L.: Forcing of secondary waves by breaking of gravity waves in the mesosphere. J. Geophys. Res.-Atmos., 107, ACL 3-1–ACL 3-7, https://doi.org/10.1029/2001JD001204, 2002.